



### 저작자표시-비영리-변경금지 2.0 대한민국

이용자는 아래의 조건을 따르는 경우에 한하여 자유롭게

- 이 저작물을 복제, 배포, 전송, 전시, 공연 및 방송할 수 있습니다.

다음과 같은 조건을 따라야 합니다:



저작자표시. 귀하는 원 저작자를 표시하여야 합니다.



비영리. 귀하는 이 저작물을 영리 목적으로 이용할 수 없습니다.



변경금지. 귀하는 이 저작물을 개작, 변형 또는 가공할 수 없습니다.

- 귀하는, 이 저작물의 재이용이나 배포의 경우, 이 저작물에 적용된 이용허락조건을 명확하게 나타내어야 합니다.
- 저작권자로부터 별도의 허가를 받으면 이러한 조건들은 적용되지 않습니다.

저작권법에 따른 이용자의 권리와 책임은 위의 내용에 의하여 영향을 받지 않습니다.

이것은 [이용허락규약\(Legal Code\)](#)을 이해하기 쉽게 요약한 것입니다.

[Disclaimer](#)



**Master of Science**

**Preparation of bio-mass derived porous carbon for  
the active materials of energy storage devices**

**The Graduate School of University of Ulsan**

**Department of Chemical Engineering  
So Eun Kim**

**Preparation of bio-mass derived porous carbon for  
the active material of energy storage devices**

Supervisor Prof. Won Mook Choi

A Dissertation

Master

by

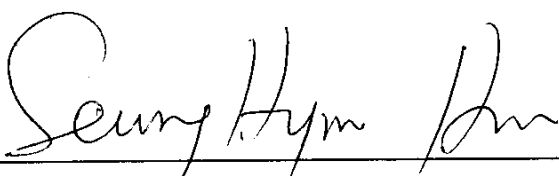
So Eun Kim

**Department of Chemical Engineering  
University of Ulsan, Korea  
February 2020**

**Preparation of bio-mass derived porous carbon for  
the active material of energy storage devices**

This certifies that the master's thesis

of So Eun Kim is approved.

  
Seung Hyun Hur

Committee Chair Prof. Seung Hyun Hur

  
Eun Suok Oh

Committee Member Prof. Eun Suok Oh

  
Won Mook Choi

Committee Member Prof. Won Mook Choi

**School of Chemical Engineering**

**University of Ulsan, Korea**

**February 2020**

# Abstract in Korean

환경 문제에 대한 인식이 높아짐에 따라 지속 가능한 에너지에 대한 관심이 증가하고 있다. 그와 동시에 에너지 수요 또한 빠르게 증가하고 있어, 환경 친화적일 뿐만 아니라 높은 효율을 가지는 에너지 저장 장치 개발이 요구되고 있다. 그 중 슈퍼커패시터는 높은 출력 밀도와 빠른 충·방전 속도, 긴 수명을 가져 전기 자동차나 휴대용 전자기기 등에 사용된다. 하지만 배터리에 비해 에너지 밀도가 낮아, 이를 향상시키기 위한 넓은 비표면적과 높은 전도성을 가진 탄소 물질에 대한 연구가 필요하다.

따라서 본 논문에서는 다음과 같은 방법으로 슈퍼커패시터용 친환경 바이오 매스 기반 탄소 소재의 제조 방법을 개발하였다. (1) 질소 분위기에서 KOH 활성화를 통해 튀밥으로부터 3D 구조의 다공성 활물질 (AC)을 제조하고, (2) 검은 콩으로 만든 두유를 수열 반응 시켜 얻은 N,S-그래핀 양자점 (N,S-GQD)을 활물질에 도핑하여 전도성을 높였다. 먼저, 상압 보다 진공에서 활성화시킨 활물질이 더 높은 비표면적을 가졌으며, 그 중 250°C에서 탄화시킨 튀밥과 KOH의 질량비가 1:3인 혼합물을 질소분위기의 600°C에서 활성화 하였을 때 (1:3-600-AC) 가장 높은 비정전용량 ( $343 \text{ F g}^{-1}$  at  $1\text{A g}^{-1}$ ) 을 보였다. 이는  $2046 \text{ m}^2 \text{ g}^{-1}$ 의 높은 비표면적을 가지는 다공성 구조로 전극과 전해액 사이의 반응 면적이 증가 되었기 때문이다. 또한, 1:3-600-AC에 N,S-GQD의 질량 비율을 달리하여 만든 활물질의 전기화학적 특성을 측정하였을 때, N,S-GQD가 3 wt% 만큼 첨가된 N,S-GQD@AC가, 가장 높은 비정전용량 ( $645 \text{ F g}^{-1}$  at  $1\text{A g}^{-1}$ )을 보였다. 이는 N,S-GQD의 질소와 황으로 인한 이온전도성의 증가와 산소 작용기로 전해액에 대한 젖음성 (wettability)이 증가했기 때문이다. 위의 방법으로 제조된 활물질을 전극에 적용하면 보다 향상된 성능을 가진 슈퍼커패시터를 가질 것으로 판단된다.

## Abstract in English

Over following decade, as the awareness of environmental problems increases, renewable energy sources have drawn great attention, while energy demand is rapidly increasing, so the development of environment-friendly and highly efficient energy storage systems becomes a huge desire. Among energy storage systems, activated carbon-based supercapacitors have high power density, rapid charging/discharging rate, and long life cycle due to physical electrolyte adsorption. Therefore, they are widely applied to electric vehicles and portable electronic devices. However, they have low energy density compared to lithium-ion batteries. The main challenge lies in engineering pore size with high surface area as well as enhancing electrical conductivity that may lead to boost the performance of supercapacitors.

In this study, we have developed a method for preparing environment- friendly biomass-based materials with outstanding capacitance for supercapacitor. Our procedure includes two main steps : (1) A porous activated carbon (AC) was prepared from puffed rice through KOH activation in a nitrogen atmosphere. And (2) N,S-graphene quantum dots (N,S-GQDs) obtained by hydrothermal reaction of black soybean milk were decorated into the activated carbon to increase the conductivity. First, the vacuum-based activation method provides a higher specific surface area than when using a furnace. And the highest specific capacitance ( $343 \text{ F g}^{-1}$  at  $1\text{A g}^{-1}$ ) was obtained at mass ratio the pre-carbonized puffed rice and KOH of 1:3 at  $600^\circ\text{C}$  (1:3-600-AC) under 20ppm  $\text{N}_2$  flow. The excellent capacitance can be attributed to that the reaction area between the electrode and an electrolyte is increased due to the porous structure having a high specific surface area ( $2046 \text{ m}^2 \text{ g}^{-1}$ ). Moreover, the electrochemical properties were measured with activated carbon made by the different mass ratios of N,S-GQD in 1:3-600-AC. Among them, 3-N,S-GQD@AC sample with 3 wt% of the

N,S-GQD showed the highest specific capacitance  $645 \text{ F g}^{-1}$  at  $1\text{A g}^{-1}$  in 6M KOH electrolyte. The high contents of nitrogen, sulfur, and oxygen functional group from N,S-GQDs improve the ion conductivity and wettability of the electrolyte and make it have a high-performance supercapacitor. This evidence indicates the potential of our N,S-GQDs@AC in practical application.

**Keywords:** *Porous carbon, Biomass, Graphene quantum dots, Supercapacitors*

# Contents

<b>Abstract in Korean and English -----</b>	I, II
<b>Contents -----</b>	IV
<b>Figure list -----</b>	VI
<b>Table list -----</b>	VII
<b>1. Introduction -----</b>	1
1.1. Energy storage devices -----	1
1.2. Type of supercapacitor -----	5
1.3. The components of EDLCs -----	7
1.4. The principle of EDLCs -----	9
1.5. Activated carbon -----	11
1.5.1 Physical activation -----	11
1.5.2. Chemical activation -----	12
1.6. Graphene quantum dots (GQDs) -----	13
1.7 Synthesis method of GQDs -----	13
<b>2. Experimental method -----</b>	15
2.1. Material Preparation -----	15
2.1.1. Preparation of puffed rice derived activated carbon -----	15
2.1.2. Synthesis of N,S-GQD solution from black soybean milk -----	17
2.1.3. Preparation of N,S-GQD@AC -----	17

2.2. Fabrication -----	19
2.2.1. Three electrode system -----	19
2.2.2. Two electrode system -----	20
2.3. Characterization -----	24
2.3.1. Morphologies -----	24
2.3.2. Physicochemical characterization -----	25
2.3.3. Chemical characterization -----	26
2.3.4. Electrochemical analysis -----	26
<b>3. Results and discussion -----</b>	<b>29</b>
3.1. Morphologies -----	29
3.2. Physicochemical characterization -----	32
3.3. Chemical characterization -----	41
3.4. Electrochemical analysis -----	47
3.4.1. Three electrode system -----	47
3.4.2. Two electrode system -----	57
3.4.3. Flexible supercapacitor -----	61
<b>4. Conclusion -----</b>	<b>66</b>
<b>5. Reference -----</b>	<b>67</b>

# Figure list

- Figure 1. Projections from the International Energy Agency's Outlook to 2035
- Figure 2. Ragon-plot comparing the power and energy density of different energy storage devices
- Figure 3. Structure of supercapacitors (a) Electrochemical double-layer capacitor (EDLC)  
(B) Pseudo-capacitor (c) Hybrid capacitor
- Figure 4. Models of the electrical double layer (a) Helmholtz model, (b) Gouy-Chapman model, and  
(c) Stern model
- Figure 5. Schematic diagram of the top-down and bottom-up methods for synthesis of GQDs.
- Figure 6. Schematic illustration of the puffed rice derived activated carbon (AC) production
- Figure 7. Schematic illustration of the N,S-GQD@AC production
- Figure 8. The components of 2032 coin cell
- Figure 9. The components of the flexible supercapacitor.
- Figure 10. SEM image of AC (a), (b) the cross-section image of pre-carbonized puffed rice (PC) (c),  
(d) 1:3-600-AC
- Figure 11. TEM images of 3wt% N,S-GQD@AC
- Figure 12. Nitrogen adsorption-desorption isotherms with and without vacuum
- Figure 13. The pore size distribution of the activated carbon with and without vacuum
- Figure 14. Specific surface area and conductivity change according to N,S-GQD mass ratio
- Figure 15. The contact angle of distilled water on the electrode coated with (a) 1:3-600-AC (b) 1wt%  
N,S-GQD@AC (c) 3wt% N,S-GQD@AC (d) 5wt% N,S-GQD@AC
- Figure 16. The pore size distribution of the activated carbon with N,S-GQD
- Figure 17. XPS spectra (a) C1s, (b) N1s of 1:3-600-AC
- Figure 18. XPS spectra (a) C1s, (b) N1s of N,S-GQD@AC
- Figure 19. XPS spectra (a) C1s, (b) N1s of N,S-GQD
- Figure 20. Electrochemical performance of AC obtained with different PC and KOH mass ratios using  
6M KOH electrolyte (a) CV at 10mV/s scan rate (B) GCD at  $1 \text{ A g}^{-1}$  current density

Figure 21. Electrochemical performance of 1:3-600-AC with 6M KOH electrolyte (a) CV at different scan rate (B) GCD at the different current density

Figure 22. Electrochemical performance of AC and different N,S-GQD mass ratios with 6M KOH electrolyte (a) CV at 10mV/s scan rate (B) GCD at  $1 \text{ A g}^{-1}$  current density

Figure 23. Electrochemical performance of 3wt% N,S-GQD@AC 6M KOH electrolyte (a) CV at different scan rate (B) GCD at the different current density

Figure 24. Electrochemical performance (CV) of 1:3-600-AC and 3wt% N,S-GQD@AC in 3M  $\text{H}_2\text{SO}_4$

Figure 25. Nyquist plots of the 1:3-600-AC and 3wt% N,S-GQD@AC with 6M KOH electrolyte

Figure 26. Nyquist plots in two cases of coin cell with 3wt% N,S-GQD@AC at  $1 \text{ A g}^{-1}$  : in open circuit potential and after 5,000 cycle repetitions

Figure 27. Cycling performance of the 3wt% N,S-GQD@AC at the current density of  $1 \text{ A g}^{-1}$

Figure 28. Electrochemical performance (GCD) of flexible supercapacitor at different current density with 3wt% N,S-GQD@AC

Figure 29. 10,000 cycle performance (GCD) of flexible supercapacitor at  $1 \text{ A g}^{-1}$  with 3wt% N,S-GQD@AC

Figure 30. Different bending angle CV performance graph of the flexible supercapacitor at 10mA/s

Figure 31. GCD measurement after 1 and 2,000 time repetitions of  $180^\circ$  bending at  $1 \text{ A g}^{-1}$

Figure 32. Red light-emitting diode (LED) lighting with flexible supercapacitor

## **Table list**

Table 1. The composition of three electrode system electrode

Table 2. The composition of the two-electrode system electrode

Table 3. The specific surface area of AC obtained at different activation temperatures.

Table 4. The specific surface area of AC obtained at different KOH mass ratio.

Table 5. The specific surface area of AC obtained at different N,S-GQD mass ratio

Table 6. The elemental composition and quantities (wt%) of 1:3-600-AC, 8wt% N,S-GQD@AC, and N,S-GQDs were obtained from XPS.

Table 7. The N and O content (wt%) of 1:3-600-AC, 8wt% N,S-GQD@AC, and N,S-GQDs obtained from XPS.

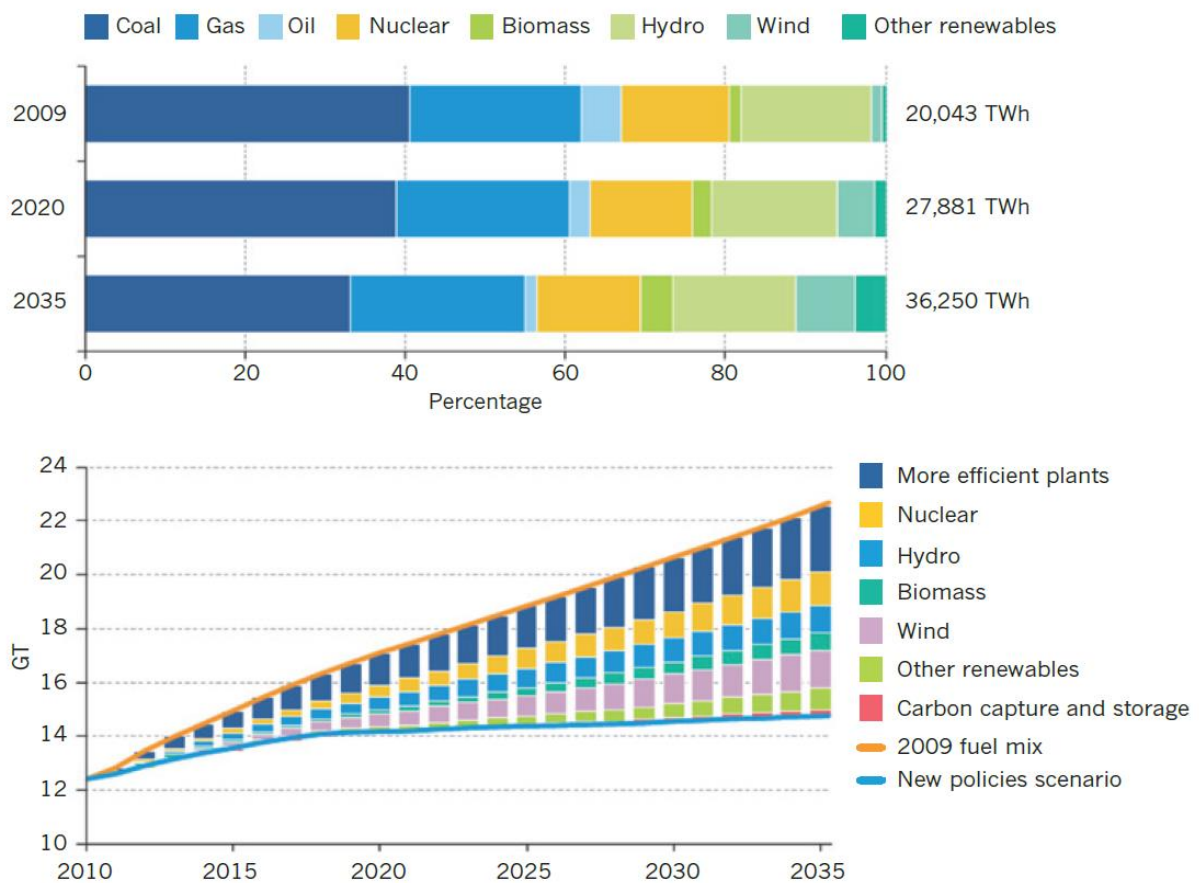
Table 8. The capacitance of AC obtained at different KOH mass ratio

Table 9. The capacitance of AC obtained at different N,S-GQD mass ratio

# **1. Introduction**

## **1.1. Energy storage devices**

During the past century, energy demand has increased by economic growth and increasing population, thus leading to huge fossil fuel consumption, which causes global climate change and environmental problems [1]. To address these issues, the United Nations Framework Convention on Climate Change (UNFCCC) was signed to reduce emissions of carbon dioxide and greenhouse gases (GHGs). With the adoption of the “Paris Agreement” in 2015, all parties to the agreement should work towards their own GHGs reduction targets from 2020 to 2030. Therefore, renewable energies from natural sources including solar, wind, geothermal, and biomass have drawn great attention as they can reduce greenhouse gas emissions [1-5]. However, most renewable energy sources have problems with continuous supply because their output fluctuates heavily depending on the location environment, weather, and time [6]. Thus, high-efficiency energy storage devices are needed to meet the continuous energy demands. Fig. 1 shows projections from the International Energy Agency’s Outlook to 2035 [1].



**Figure 1. Projections from the International Energy Agency's Outlook to 2035 [1]**

Nowadays, due to effectiveness in energy conversion and storage, many efforts have been invested in development of electrochemical energy systems including fuel cells, lithium-ion batteries, and supercapacitors [7]. Fuel cells are devices that produce electricity through the redox reaction of hydrogen and oxygen fuels supplied from outside. To use renewable energy in fuel cells, a device that converts it to hydrogen fuel is required, and electricity must be re-produced through fuel cells [8]. However, Lithium-ion batteries are secondary cells. They can store electrical energy obtained from renewable sources as chemical energy by reversible electrochemical redox reaction and vice versa. But the redox reaction mechanism leads to long charge/discharge rate and low stability, which limits their utilization [9]. In addition, battery electrode materials such as cobalt, nickel, and lithium are expensive and harmful to the environment, making it difficult to dispose of waste batteries [10]. In contrast, electrode materials of supercapacitors are mostly composed of carbon-based materials, which are relatively low-cost and environment-friendly. Besides, supercapacitors offer the benefits of high power density, rapid charge/discharge rate, and high cycling stability. But supercapacitors possess low energy density compared to lithium-ion batteries. Fig. 2 presents Ragon-plot comparing the power and energy density of different energy storage devices [11]. Currently, most research is focused on biomass-derived activated carbons to enhance the performance of supercapacitors. Because biomasses are abundance, low-cost, and environmentally friendly. Many other biomasses have been used as sources for activated carbon such as almond shells, walnut shells [12], coconut shells [13, 14], sugar cane [15], cumin plant [16], as the precursor. In this study, puffed rice is chosen as a precursor to developing biomass activated carbon for preparing environment-friendly materials with outstanding capacitance for supercapacitor, because rice has a huge available resource and so popular in many aspects of Korean life.

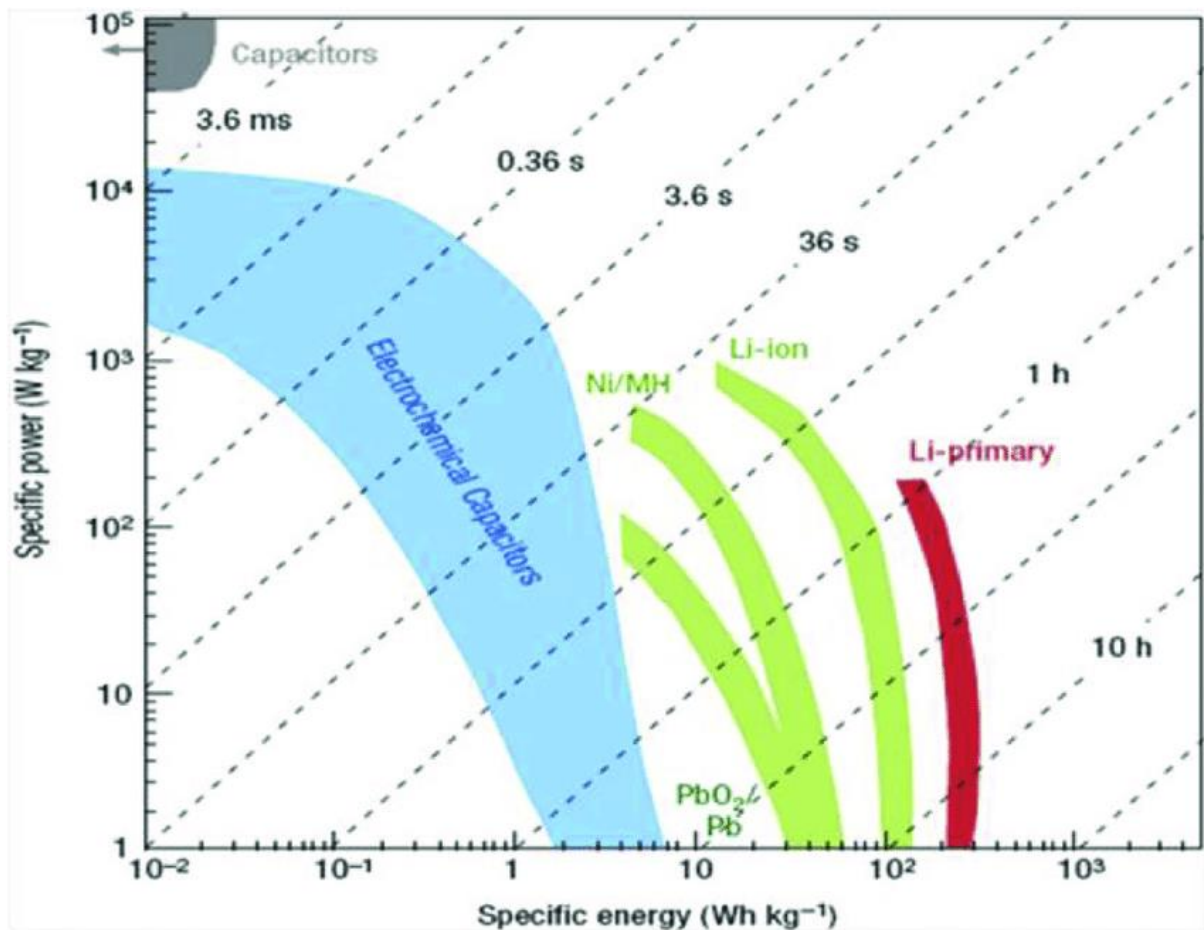
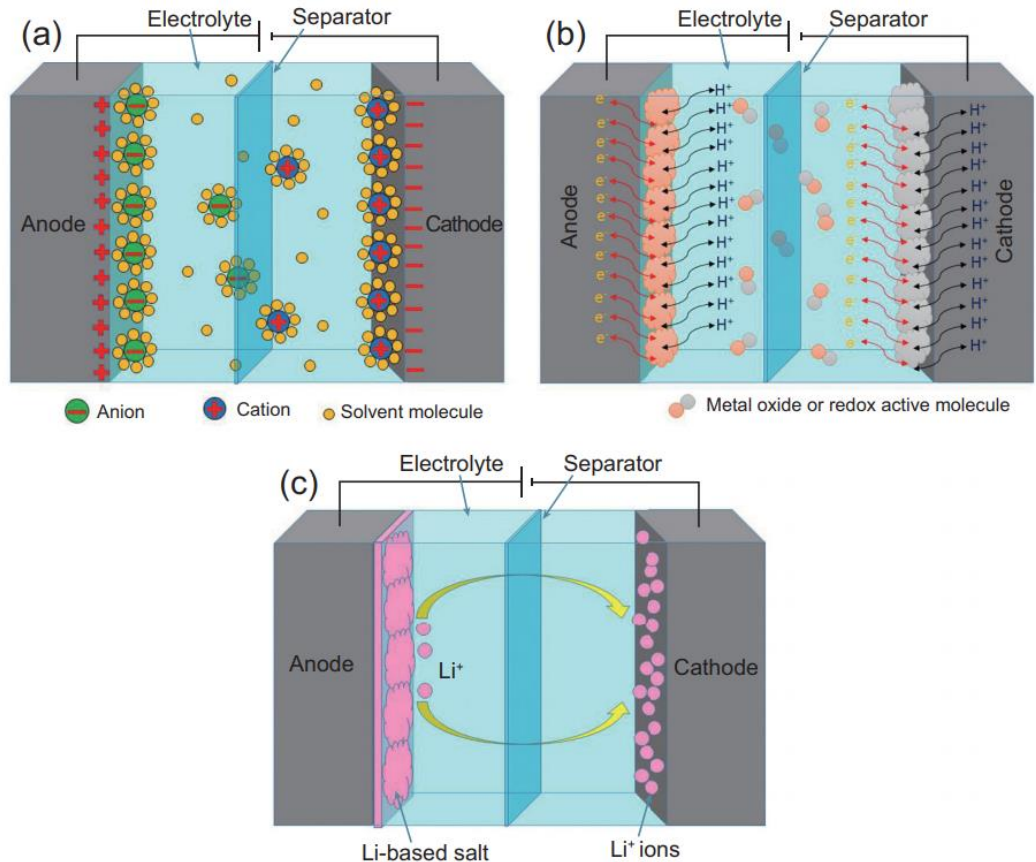


Figure 2. Ragon-plot comparing the power and energy density of different energy storage devices [11]

## **1.2. Type of supercapacitors**

Supercapacitors also referred to as electrochemical capacitors, can be classified into three types according to their charge storage mechanism: pseudo-capacitor and electrochemical double-layer capacitor (EDLC), and Hybrid capacitor. Fig. 3 shows the structure of supercapacitors [17]. Pseudo-capacitors are asymmetric cells, and metal oxides ( $\text{RuO}_2$ ,  $\text{MnO}_2$ , and  $\text{TiO}_2$ , etc.) [18], or conductive polymers (polyaniline, polythiophene, polypyrrole, and polyacetylene, etc.) [19, 20] are used as electrode materials. Like batteries, there are charged or discharged by reversible redox reactions occurring on the electrode surface. Hence, this redox reaction allows for lower cycling stability and power density compared with EDLCs. Symmetric EDLCs store energy through the physical adsorption/desorption of ionic charges on the surface of active material. Thus they are widely applied to electric vehicles, memory back-up systems, and smart grids that require high power density. [21, 22] Hybrid capacitors are asymmetric cells that combine pseudo capacitor and EDLC. Graphite or lithium titanium oxide (LTO) is applied as the anode and carbon materials are applied as the cathode. The charging/discharging rate is limited by the slow diffusion rate of the lithium ions in an electrolyte, which leads to a low power density.

In this study, we will focus on symmetric EDLCs.



**Figure 3. Structure of supercapacitors (a) Electrochemical double-layer capacitor (EDLC)  
(B) Pseudo-capacitor (c) Hybrid capacitor [17]**

### **1.3. The components of EDLCs**

The symmetric EDLCs consist of two identical electrodes, a current collector, electrolytes, and a separator. As electrode materials, porous carbon-based materials, especially activated carbons, are used and coated on current collectors with a binder. The current collector is made of aluminum foil and nickel foam. They support the carbon materials and transfer charge to the carbon electrodes or external circuit during the charge-discharge process. Therefore, it should have high electrical conductivity, low resistance with carbon materials.

[23]

Electrolytes, consisting of salt and solvent, are mediums that allow ions to flow from one electrode to another. There are aqueous electrolytes and organic electrolytes. Aqueous electrolytes can be grouped into acidic, alkaline, and neutral salts such as sulfuric acid ( $H_2SO_4$ ), potassium hydroxide (KOH), and potassium chloride (KCl). These salts have high ionic conductivity, which can increase capacitance [21]. But, the operating voltage is limited to 1.0 V due to the decomposition of water. On the other hand, Organic electrolytes using organic solvents provide a high potential window up to 2.5-2.7V. Organic electrolytes include organic solvents such as acetonitrile (ACN), dimethyl carbonate (DMC), ethylene carbonate (EC), or propylene carbonate (PC), and conducting salts such as quaternary ammonium, hexafluorophosphate ( $PF_6^-$ ), or tetrafluoroborate ( $BF_4^-$ ). Among them, tetraethylammonium tetrafluoroborate (TEABF<sub>4</sub>) dissolved in the aprotic solvent ACN or PC solvent is commonly used. However, organic electrolytes have lower ion conductivity and higher equivalent series resistance (ESR) compared to aqueous electrolytes, which can lead to lower capacitance [24].

The separator is a porous membrane placed between two electrodes to prevent short circuits. Therefore, separator materials must have high ion permeability and high electronic resistance. It should also possess high mechanical strength to prevent decomposition during ions penetration and must be chemically stable without reacting to the electrode materials and electrolytes [25]. Filter paper and cellulose separators are used with organic electrolytes. Ceramic or glass fibers and porous polymer membranes (polypropylene (PP), polyethylene (PE)) are used with high concentration aqueous electrolytes.

## 1.4. The principle of EDLCs

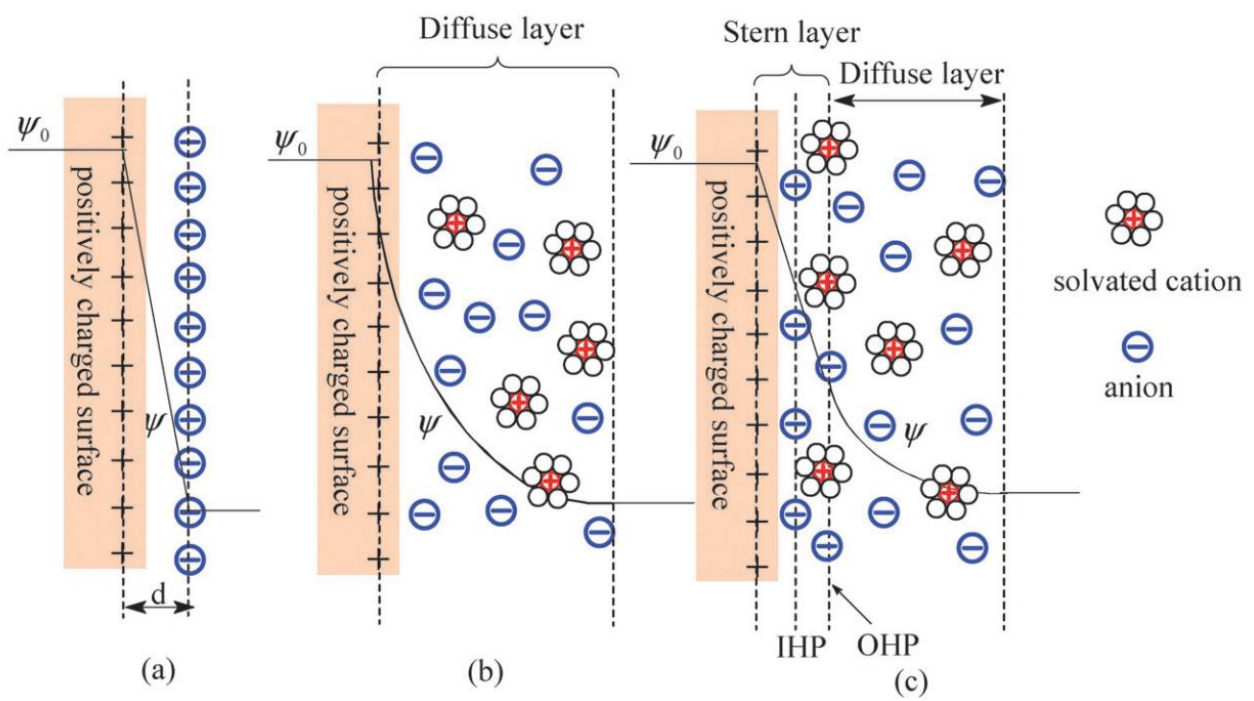
In EDLCs, charges are stored by the electric double layer. When voltage is applied to EDLCs, the solvent molecules are adsorbed on the electrode surface and polarized by the electric charge, forming a dipole moment. These solvent molecules act as a dielectric. Ionic charges then migrate towards the electrode of opposite polarity and accumulate until the potential difference of the electrode is in equilibrium with the applied voltage. This layer, in which electronic and ionic charges are aligned in parallel, is called the electric double layer.

Fig 4. presents models of the electrical double layer at a positively charged surface [17, 26]. Conversely, during the discharge process, the ionic charges diffuse back into the electrolyte.

Since charges are stored electrostatically without a chemical reaction, the capacitance (C) is proportional to the specific surface area (A) and inversely proportional to the distance (d) of the electric double layer. It can be expressed in the following formula:

$$C = \epsilon_0 \epsilon_r \frac{A}{d} \quad (1)$$

Here,  $\epsilon_0$  is permittivity of vacuum ( $8.854 \times 10^{-12} \text{ F g}^{-1}$ ),  $\epsilon_r$  is the relative permittivity, and d is electric double layer thickness. Therefore, electrode material with appropriate pore size, high porosity, and large specific surface area is used to improve the specific capacitance. In this study, the main challenge lies in engineering pore size with a high surface area that may lead to boost the performance of supercapacitors.



**Figure 4. Models of the electrical double layer (a) Helmholtz model, (b) Gouy-Chapman model, and (c) Stern model [26].**

## 1.5. Activated carbon

In symmetric EDLCs, carbon-based materials are mostly used as electrode materials. This is because carbon can easily obtain microstructures and exist in various forms and dimensions, including activated carbons (ACs), carbon fibers, carbon nanotubes (CNTs), and graphenes [7, 17, 26]. Among them, activated carbons have been mostly utilized due to their large specific surface area, and porous structure. Porous activated carbon is prepared via chemical and physical activation process.

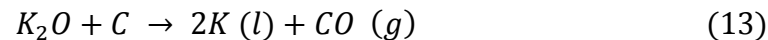
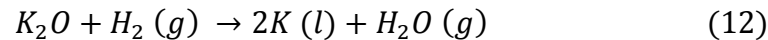
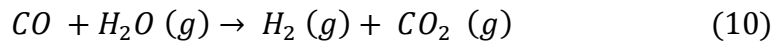
### 1.5.1 Physical activation

Physical activation involves two steps: pyrolysis and gasification reaction. In the process of pyrolysis, also known as carbonization, carbon materials are heated to a high temperature in an inert atmosphere to remove oxygen and hydrogen elements. Then the pores are formed through the gasification reaction with oxidizing gases such as steam, carbon dioxide, or air [14, 27]. The following mechanisms are the physical activation reaction with carbon dioxide and steam: [28]



### 1.5.2. Chemical activation

In the chemical activation, carbon materials are impregnated by an acidic or basic activator such as potassium hydroxide (KOH), zinc chloride ( $ZnCl_2$ ), and phosphoric acid ( $H_3PO_4$ ). Activation and carbonization then proceed simultaneously in an inert gas at a high temperature [14, 29]. In general, KOH activation is applied to supercapacitor electrode materials preparation. This is because pore size distribution can be controlled by different amounts of KOH and various activation temperatures [29] and more thermally stable than  $ZnCl_2$  or  $H_3PO_4$  activation [30]. Unlike  $ZnCl_2$  and  $H_3PO_4$ , which act as dehydrating agents, KOH act as an oxidizing agent [29]. And the activation reaction of KOH is as follows [31, 32] :



KOH decomposes into  $K_2O$  and  $H_2O$  at high temperatures and these react with the carbon to generate pores on the carbon surface. The resulting potassium compound and residual KOH are washed in subsequent steps. In this study, we obtained puffed rice derived activated carbon through KOH activation.

## **1.6. Graphene quantum dots (GQDs)**

Graphene quantum dots (GQDs) are nanoscale graphene with a size of less than 100nm. GQDs are considered the most promising carbon-based nano-materials due to their low toxicity, photoluminescence properties, great electronic properties, high surface area, chemical, and physical stability. GQDs are applied in various fields such as photodetectors [33, 34], photocatalysis [35], solar cell [36], and energy storage systems [37, 38] by utilizing their characteristics.

## **1.7. Synthesis method of GQDs**

Synthesis of GQDs can be classified into “top-down” and “bottom-up” methods. Fig. 5 shows a schematic diagram of the top-down and bottom-up methods for the synthesis of GQDs. Top-down method approach is to cut carbon materials including graphene, fullerenes, carbon nanotubes, etc. into GQDs through physical, chemical, or electrochemical techniques. This method involves the exfoliation and decomposition of carbonaceous materials by electrochemical oxidation [39], hydrothermal [40], or solvothermal [41] cutting, etc. Bottom-up method is realized by the carbonization of small organic molecules from polycyclic aromatic compound or fullerene via cage opening of fullerene [42], carbonization [43], hydrothermal [37], or microwave-assisted hydrothermal treatment [44]. Recently, there is much interest in bottom-up method that uses low cost, nontoxic precursors, and allows uniform size control. In this study, N,S-GQDs were synthesized from black soybean milk by a bottom-up method.

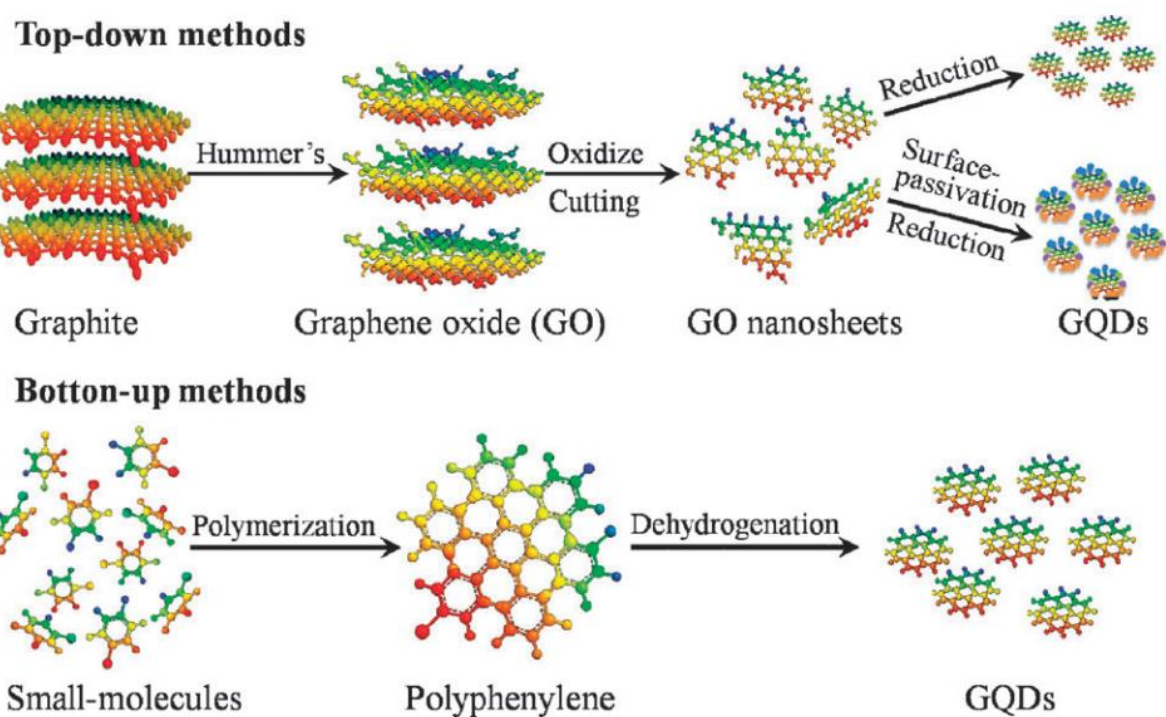


Figure 5. Schematic diagram of the top-down and bottom-up methods for synthesis of GQDs.

[45]

## **2. Experimental methods**

### **2.1. Material Preparation**

#### **2.1.1. Preparation of puffed rice derived activated carbon**

In this study, puffed rice was used as a biomass precursor of activated carbon. The puffed rice derived activated carbon (AC) can be prepared through the following chemical treatments. Firstly, puffed rice was pre-carbonized at 250°C in a nitrogen atmosphere furnace for 1 hr. Pre-carbonized puffed rice (PC) was impregnated with different KOH mass ratios. (The mass ratio of PC: KOH is 1:2, 1:3, 1:4, and 1:5.) And It was chemically activated and carbonized under the vacuum control by using chemical vapor deposition (CVD) equipment at 500°C, 600°C, 700°C, and 800°C for 15 min. During the activation process, 20ppm nitrogen gas flows continuously. After cooling to room temperature, residual KOH and potassium compounds were removed from the sample with 10% hydrochloride (HCl) solution, and samples were washed several times with distilled water until the pH becomes neutral. Finally, the puffed rice derived activated carbon (AC) is dried in an oven. The obtained ACs were denoted as 1:X-Y-AC, where X and Y represent the mass ratio of KOH and the activation temperature, respectively. Fig. 6 presents the production of activated carbon from puffed rice.



**Figure 6. Schematic illustration of the puffed rice derived activated carbon (AC) production**

### **2.1.2. Synthesis of N,S-GQD solution from black soy milk**

Nitrogen (N) and sulfur (S)-doped graphene quantum dots (N,S-GQD) were synthesized by direct heat treatment of black soy milk containing N and S. At this time, a carbon skeleton is made from the sugar in black soymilk. Typically, 1 ml black soy milk was dispersed in 50 ml distilled water by stirring for 30 min. The mixture then was transferred into 100 ml Teflon line and was sealed in stainless steel autoclave. The autoclave was kept 160°C for 4 hr. After the hydrothermal reaction, the yellow solution was obtained. The final product was collected by purifying in a dialysis bag (3,000 Da) for 24 hr to remove all impurities.

### **2.1.3. Preparation of N,S-GQD@AC**

N,S-GQD solution is added to 1:3-600-AC in the amount of 1 wt%, 3 wt%, 5 wt%, and 8 wt%. The samples were stirred in 300 ml of distilled water for 24 hr. And it was centrifuged to separate distilled water and samples. The remaining distilled water in the samples was removed by freeze-drying at 80°C for 24 hr. The samples were completely frozen before starting the drying process to sublimate the ice into water vapor. 1:3-600-AC decorated with N,S-GQDs is obtained and denoted as Z-N,S-GQD@AC. Where Z represents the amount of N,S-GQDs. Fig. 7 shows the production of N,S-GQD@AC from black soybean milk.

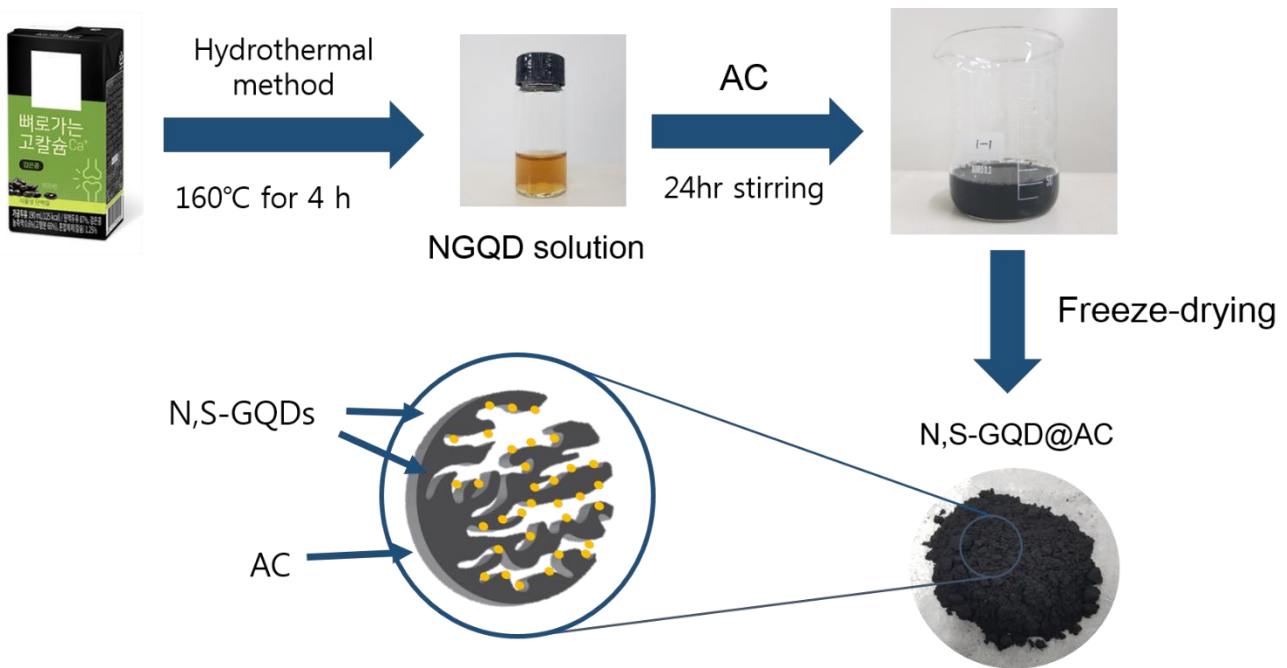


Figure 7. Schematic illustration of the N,S-GQD@AC production

## 2.2 Fabrication

### 2.2.1. Three electrode system

Prepared samples were individually used as active material. Super-p was used as a conductive agent. Carboxyl methyl cellulose (CMC) and styrene-butadiene rubber (SBR) were used as binders. The slurry mixture was composed of 85 wt% active material, 8 wt% super-p, 2 wt% CMC and 5 wt% SBR. Distilled water was used as a solvent to adjust the viscosity of the slurry. In order to compare the performance of prepared active material, commercial activated carbon YP50F (Kuraray Chemical Co., Ltd., Japan) was used as a reference.

Three different electrodes are used in three electrode system: the working electrode, the counter electrode, and the reference electrode. The working electrode is the electrode on which the reaction of interest occurs. The prepared slurry was coated on the working electrode. The potential and current are measured at the working electrode. The counter electrode, also called an auxiliary electrode, is an electrode used to balance the reactions occurring at the working electrode, and its potential is not measured. The reference electrode is an electrode that controls and measures the potential applied to the working electrode. In this study, glassy carbon as the working electrode, A platinum wire as a counter electrode, a calomel electrode, and Ag/AgCl electrode as a reference electrode were used. And the 6M KOH solution and 3M H<sub>2</sub>SO<sub>4</sub> were used as electrolytes.

## **2.2.2. Two electrode system**

### **2.2.2.1. Fabrication of CR2032 coin cell**

The electrode slurry was prepared by mixing 85 wt % ACs, 10 wt % polytetrafluoroethylene (PTFE), and 2 wt % acetylene black in 2 ml NMP. Then, the slurry solution was cast on the nickel foam by a doctor blade. The sample was dried at 45°C in vacuum condition for 24h. Two symmetric electrodes were used. One of the electrodes was used as a working electrode, and the other as counter electrodes. Finally, CR2032-type coin cells were assembled in an Ar-filled glove box with oxygen content less than 1 ppm using a nonwoven polypropylene mat (MPF 30AC) as the membrane to separate two working electrodes with 6M KOH as the electrolytes. The loading mass is around 1.8 mg/cm<sup>2</sup>. The gasket was used to prevent electrolyte leakage. Spacer and wavering were used to fill the empty spaces. Fig. 8 shows the components of the 2032 coin cell.

### **2.2.2.2. Fabrication of flexible supercapacitor**

The obtained above slurry solution was cast on carbon clothes by using a doctor blade. The electrode then was dried in a vacuum oven at 60°C for 24h. The PVA-KOH polymer gel was prepared by dissolving 3 g of PVA in 6 m KOH (30 mL) of DI water. The mixtures were stirred continuously under 90°C until the clear gel was achieved. The N,S-GQD@AC electrode, and PVA-KOH as the membrane were stacked to form the flexible supercapacitor. The assembled device area is 5x3 cm (1.5 cm<sup>2</sup>). Fig. 9 includes the structure of the flexible supercapacitor.

**Table 1. The composition of three electrode system electrode**

	1:3-600-AC or N,S-GQD@AC	Super-p	Binder	
			1% CMC	SBR (TSC 40%)
Ratio	85%	8%	2%	5%

**Table 2. The composition of two-electrode system electrode**

	1:3-600-AC or N,S-GQD@AC	Acetylene black	PTFE	NMP
Ratio	85%	2%	10%	2ml

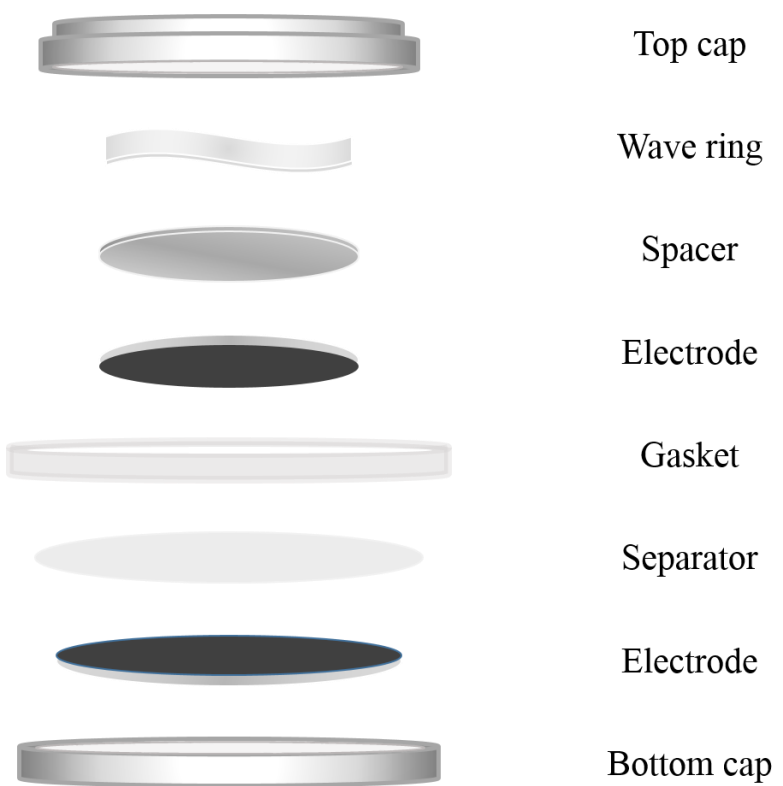


**Figure 8. The components of 2032 coin cell**

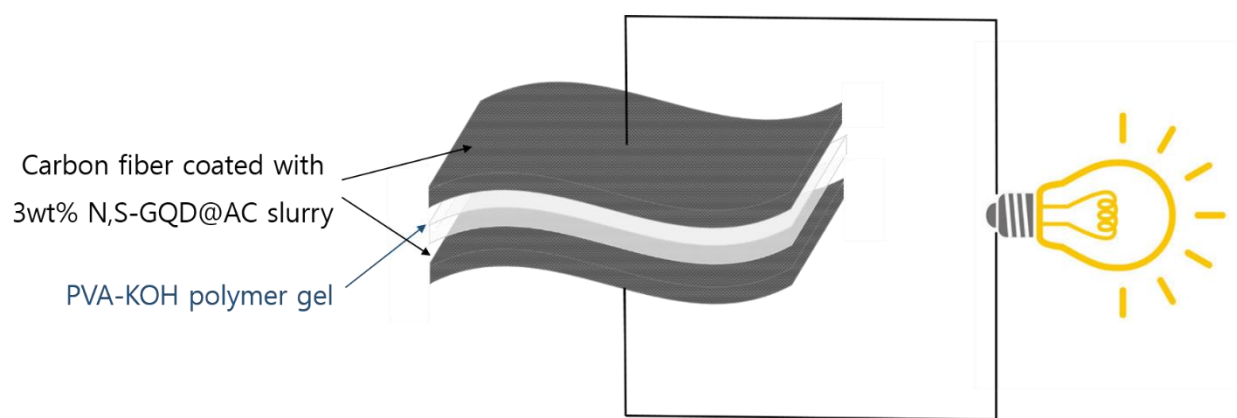


**Figure 9. The components of the flexible supercapacitor.**

## **2.3. Characterization**

### **2.3.1. Morphologies**

Field-emission scanning electron microscopy (FE-SEM) is utilized to recognize the surface topography of the specimen. In a high vacuum state, an electron beam is generated with the effect of emitting electrons by applying a high electric field to the metal surface. When the electron beam enters the specimen, secondary electrons are generated on the specimen surface. By detecting this electric signal, the surface images were obtained [46]. In this study, the surface morphologies of PC and 1:3-600-AC were observed with FE-SEM (JEOL JSM - 6500F). And transmission electron microscopy (TEM) is utilized to analyze the internal structure of the specimen. In a vacuum, the electron beam penetrates the sample loaded on the grid. The transmitted electron beam is magnified through the lens. The image is acquired with a fluorescent screen or photosensitive sensor. FE-SEM (JEOL 6400) was used to investigate N,S-GQD in 1:3-600-AC

### 2.3.2. Physicochemical characterizations

The surface area of AC and N,S-GQD@AC was measured by the nitrogen adsorption analysis, utilizing Quantachrome Quadrasorb EVO. The samples were degassed at 300 °C for 40 hr before measurements (Quantachrome XeriPrep degasser).

Nitrogen gas was adsorbed or desorbed as a monolayer on the sample surface at 77K. The volume of adsorbed gas depends on the relative pressure ( $P/P^0$ ). In this study, adsorbed nitrogen gas was measured from  $P/P^0=0.1$  to  $P/P^0=0.99$ . The volume of adsorbate gas at  $P/P^0$  ( $V_a$ ) can be obtained by the following Brunauer-Emmett-Teller measurement (BET) equation. [47]

$$\frac{1}{V_a \left( \frac{P}{P_0} - 1 \right)} = \frac{1}{V_m C} + \frac{C - 1}{V_m} \times \frac{P}{P_0} \quad (14)$$

$V_a$  is the volume of gas adsorbed at standard temperature and pressure (STP), and  $C$  is BET constant. From the  $V_m$ , the total surface area of the sample ( $S_t$ ) can be determined.

$$S_t = \frac{v_m N s}{V} \quad (15)$$

$N$  is Avogadro's number ( $6.02 \times 10^{23}$  molecules mol<sup>-1</sup>),  $s$  is the cross-section area of the adsorbed gas molecule, and  $V$  is the molar volume of adsorbed gas. Finally, a specific surface area ( $S_{BET}$ ) is calculated from the  $S_t$  and mass of sample ( $a$ ).

$$S_{BET} = \frac{S_t}{a} \quad [m^2 g^{-1}] \quad (16)$$

And the pore size distributions and pore volume were calculated by the density functional theory (DFT).

### **2.3.3. Chemical characterizations**

#### **2.3.3.1 X-ray photoelectron spectroscopy (XPS)**

XPS (ESCALAB 250XI) was performed to know the elemental composition and chemical state of elements within PC, 1:3-600-AC, and N,S-GQD@AC. When an Al  $\text{k}\alpha$  x-ray is irradiated on the sample, photoelectrons are emitted from the sample surface. The kinetic energy (KE) of the emitted electrons is measured with an electron energy analyzer. Elemental information can be determined from the binding energy and intensity of the photoelectron peaks.

### **2.3.4. Electrochemical analysis**

#### **2.3.4.1 Cyclic voltammetry (CV)**

Cyclic voltammetry (CV) was conducted with a three-electrode system. CV test is a method of analyzing the reactions occurring on the electrode surface. Current is measured while changing the voltage at a constant rate. When the set potential is reached, the potential of the working electrode increases in the opposite direction, returning to the initial potential. It is shown as a plot of current versus potential. The prepared samples were performed at voltages ranging from -1.0V to 0V at various scan rates (VSP, BioLogic Science Instruments).

#### 2.3.4.2 Galvanostatic charge/discharge (GCD)

Galvanostatic charge/discharge (GCD) was conducted with a three electrode system and two-electrode system. GCD test is a method of measuring a change in voltage over time by applying a constant current (galvanostatic). Continuous charging and discharging are possible within the set potential limits. And the capacitance and cycle stability of the samples can be obtained. In this study, the capacitance was measured by various current densities in the voltage range of -1.0V to 0V using three-electrode systems (VSP, BioLogic Science Instruments). Cycling stability was performed by 10mA F<sup>-1</sup> in the voltage range 0V to 1.0V using coin cells.

The specific capacitance (C) from GCD is calculated by the following equations:

$$C = \frac{2I\Delta t}{m\Delta V} \quad (17)$$

Here, I is current,  $\Delta t$  is the discharge time, V is the operating voltage window, and m is the mass of active material in the single electrode.

And The energy density (E) can be calculated by the following equation.

$$E = \frac{1}{2} CV^2 \quad (18)$$

Here, V is the operating voltage window and is dependent on the selected electrolyte.

#### 2.3.4.3 Electrochemical impedance spectroscopy (EIS)

Electrochemical impedance spectroscopy (EIS) was measured with symmetric coin cells. EIS is a method of measuring resistance by applying alternating current (AC) signals with different frequencies to a cell. Impedance is written as a real impedance component ( $Z'$ ) and an imaginary impedance component ( $Z''$ ) for each applied frequency. And electrochemical data is presented as a Nyquist plot. In this study, cells made with a 3 wt% N,S-GQD@AC electrode were conducted at OCV over from 1 mHz to 100 kHz with 5 mV.

#### 2.3.5 Analysis of flexible supercapacitor

To investigate the performance of the flexible supercapacitor, GCD was measured at different current densities and also measured for 10,000 cycles at a  $1\text{A g}^{-1}$ . The CV test was performed at 5mV/s at different bending angles, and after bending 2,000 times at  $180^\circ$ , the CD test was performed at  $1\text{A g}^{-1}$ .

### **3. Results and discussion**

#### **3.1. Morphologies**

Morphologies and structure of PC and AC were characterized by field-emission scanning electron microscopy (FE-SEM). Fig. 10 a and b present the cross-section image of pre-carbonized puffed rice (PC). As we can see in these images, the PC has honeycomb structures with a smooth surface. This structure is formed by the “puffing effect” that occurs when the internal pressure of rice increases by heat and the pressure is suddenly released [48, 49]. This can lead to a high specific surface area. Fig. 10 c and d present the structure when PC immersed in 6M KOH was carbonized and activated under vacuum control in 600°C furnace. It was confirmed that hierarchical micropores with uniform sizes were formed on the surface due to KOH activation. These micropores not only provide a large specific surface area but also give a high pore volume to the active materials.

The internal structure of N,S-GQD@AC was characterized by transmission electron microscopy (TEM). Fig. 11 a shows TEM images of N,S-GQDs distributed over the 1:3-600-AC surface. It can be seen that N,S-GQDs are not aggregated with each other and are well dispersed on the Ac surface. Fig. 10 b includes a magnified N,S-GQD on the AC surface. There are micropores on the AC surface and N,S-GQDs have a uniform size of 2.5nm. And it also indicates that the spacing grid is 0.25nm

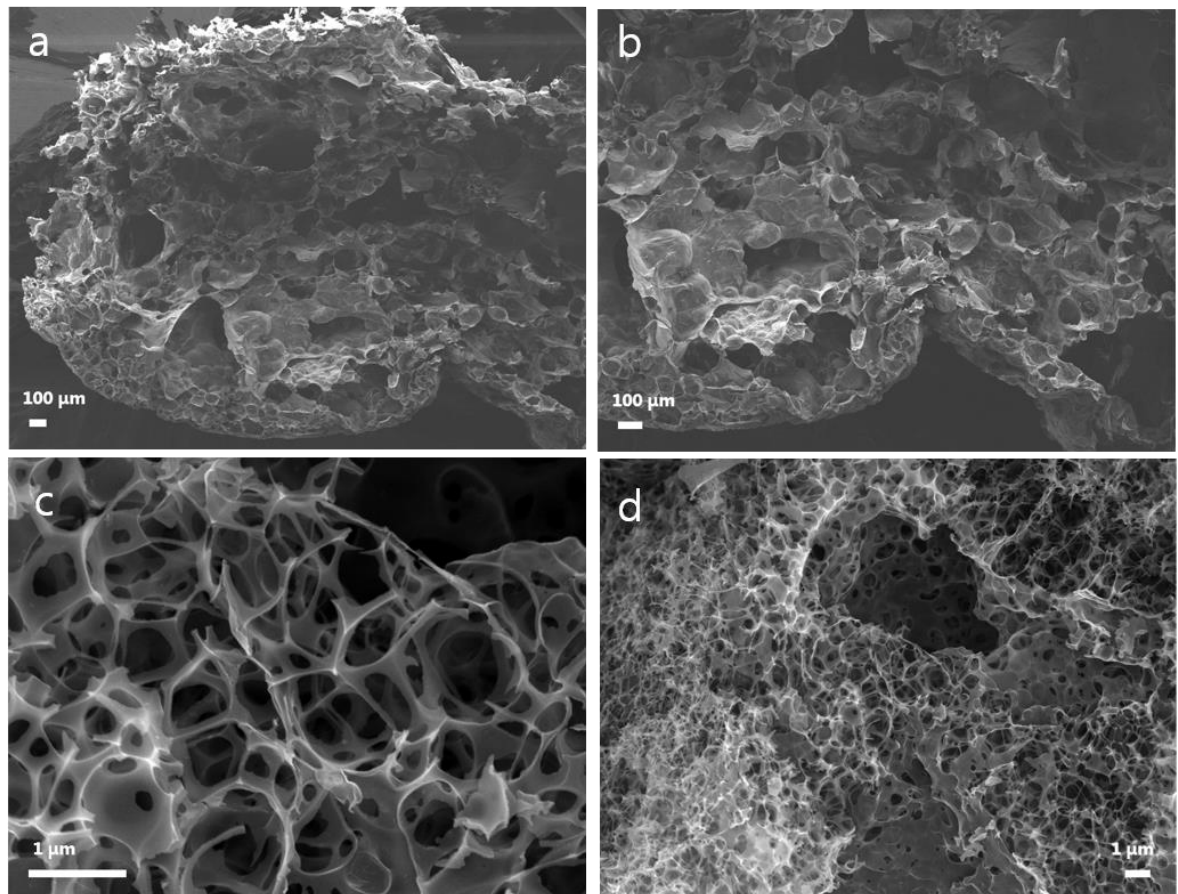


**Figure 10. SEM image of AC (a), (b) the cross-section image of pre-carbonized puffed rice (PC) (c), (d) 1:3-600-AC**

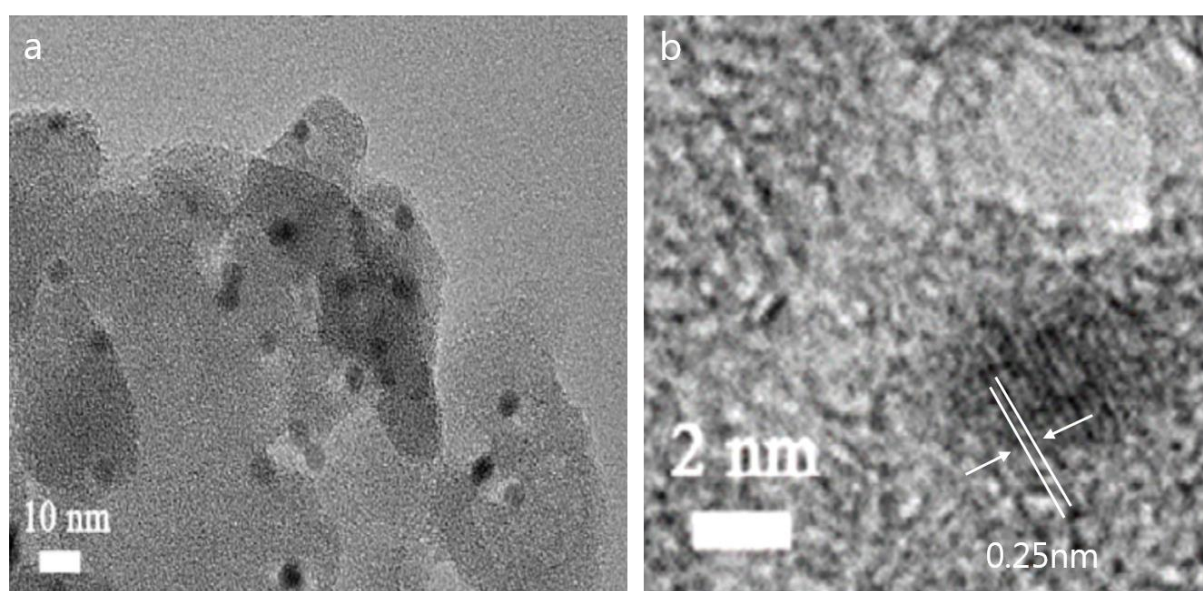


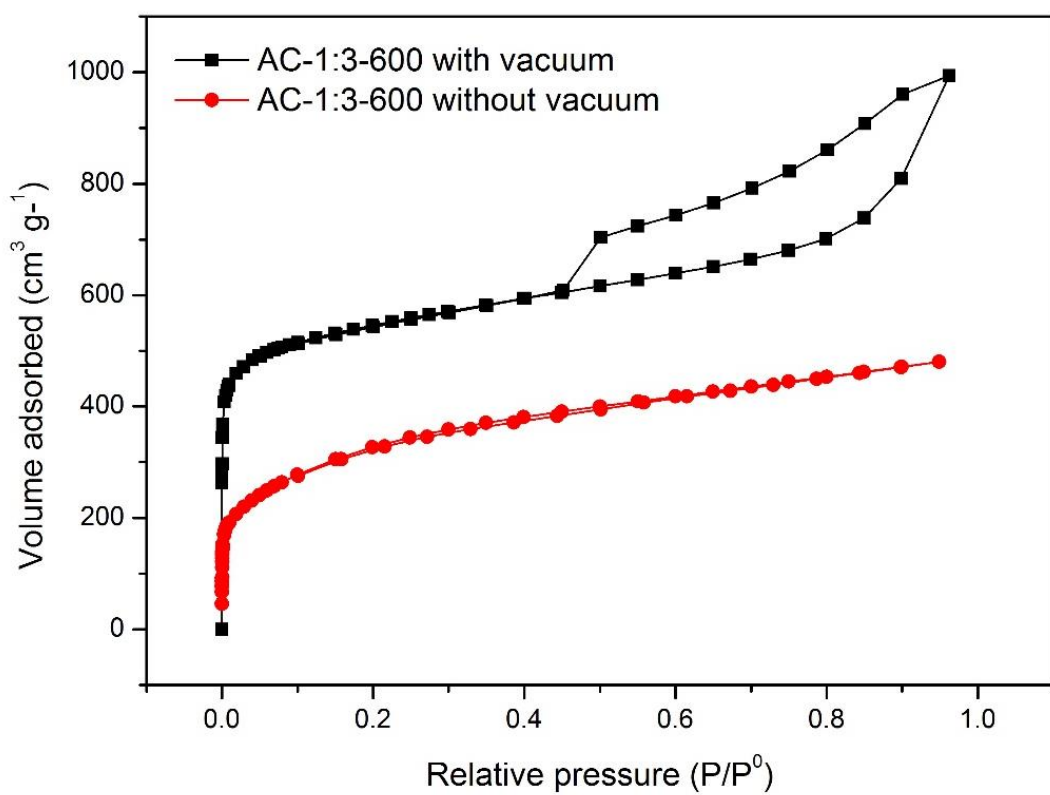
**Figure 11. TEM images of 3wt% N,S-GQD@AC**

### **3.2. Physicochemical characteristics**

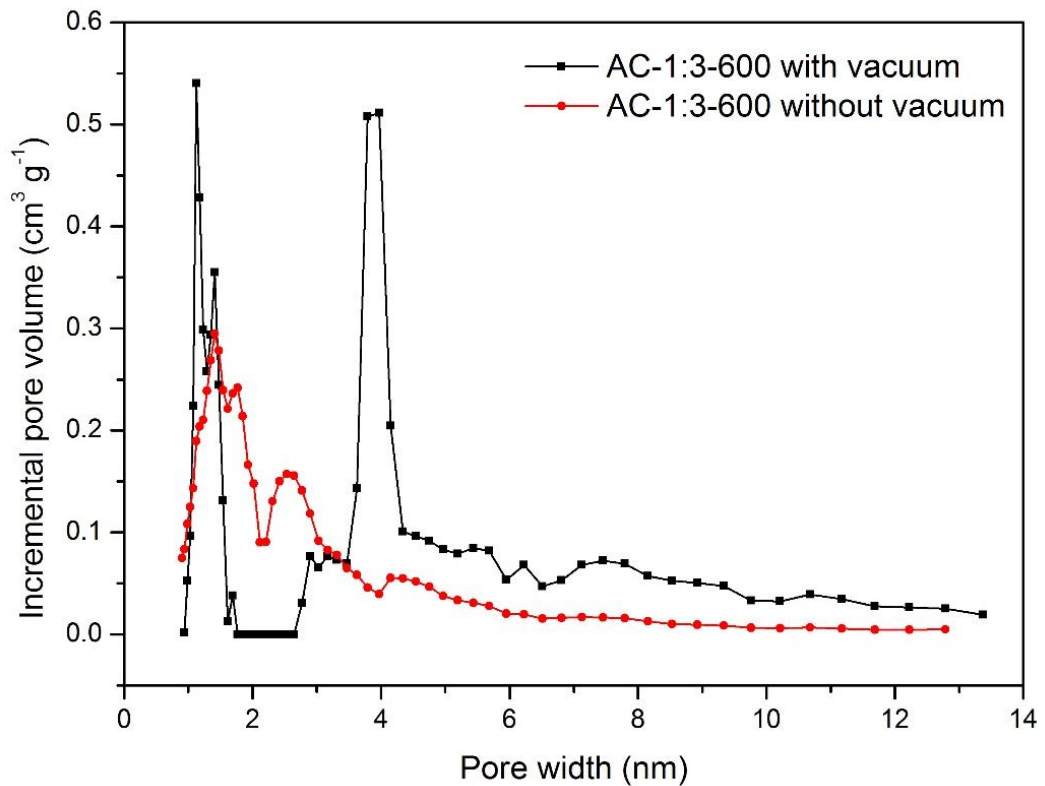
The prepared samples were characterized by Brunauer-Emmett-Teller measurement (BET) to investigate the influence of the specific surface on the electrochemical performance. Fig.12 displays isotherms of the activated carbon obtained with vacuum and without vacuum. Both of them show type I adsorption isotherms, but the AC obtained under vacuum has a hysteresis loop. The appearance of the loops indicates the existence of a hierarchical pore structure, which means that the 3D structure of the puffed rice was preserved when activated and carbonized in a vacuum. Hierarchical pore structure provides fast interfacial ion-transport and efficient ion accessible surface area for charge storage.

Fig. 13 presents the pore size distribution of the AC with and without vacuum. The observed pore size distribution of the vacuum-controlled AC confirms the presence of two peaks, micropores and mesopores. However, the pore distribution of AC obtained without vacuum cannot see narrow peaks and is evenly distributed from 1 nm to 4nm. Therefore, through vacuum control, activated carbon having a large specific surface area and large pore volume (Table. 4), as well as suitable pores, can be obtained.

The specific surface area and total pore volume of AC using different activation temperatures (500°C, 600°C, 700°C, 800°C) and KOH mass ratio (1:2, 1:3, 1:4, 1:5) are summarized in Table 3, 4. When the PC: KOH ratio was 1:3, and the activated temperature is 600°C, 1:3-600-AC has the highest specific surface area and pore volume.



**Figure 12. Nitrogen adsorption-desorption isotherms with and without vacuum**



**Figure 13. Pore size distribution of the activated carbon with and without vacuum**

**Table 3. The specific surface area of AC obtained at different activation temperatures.**

Sample	$S_{BET}$ ( $m^2 g^{-1}$ )
1:4-500-AC	672
1:4-600-AC	1,694
1:4-700-AC	1,090
1:4-800-AC	950

**Table 4. The specific surface area of AC obtained at different KOH mass ratio**

Sample	$S_{BET}$ ( $m^2 g^{-1}$ )	Pore volume ( $cm^2 g^{-1}$ )
YP-50F	1336 [50]	0.82 [50]
1:2-600-AC	902	-
1:3-600-AC	2,071	1.538
1:4-600-AC	1,694	-
1:5-600-AC	1,163	-
1:3-600-AC without vacuum	1,190	0.668

Fig. 14 includes the change of specific surface area and conductivity according to the N,S-GQD mass ratio. Conductivity was measured using an electrode coated with a slurry containing 93% of N,SGQD@AC, 2% of 1% CMC, and 5% of SBR. 1:3-600-AC has the lowest ionic conductivity of 0.546 S/cm. The ionic conductivity of the 1wt%, 3wt%, and 5wt% N,S-GQDs ratio are  $1.26 \text{ S cm}^{-1}$ ,  $2.45 \text{ S cm}^{-1}$ , and  $2.65 \text{ S cm}^{-1}$ , respectively. The ionic conductivity of 3wt% and 5wt% is not significantly different, but the specific surface area of 3wt% is much larger compared to 5wt%.

The contact angle when distilled water was dropped onto an electrode coated with 1:3-600-AC and N,S-GQD@AC is presented in Fig.15. Electrode coated with 1:3-600-AC (0 wt%) has the largest contact angles of  $85.38^\circ$  and  $85.57^\circ$  (Fig. 15 a), and electrode coated with 5wt% N,S-GQD@AC has the smallest contact angles of  $33.21^\circ$  and  $31.18^\circ$  (Fig. 15 d). Therefore, it can be seen that the contact angle decreases as the ratio of N,S-GQD increases, which means that the wettability of the electrode to distilled water improves.

Meanwhile, in the Table. 5, as the ratio of N,S-GQD increases, the specific surface area, and pore volume decrease. It is because N,S-GQD blocks the pores of AC of 1 to 4nm size, as shown in Fig. 16. Blocked AC pores reduce the diffusion of electrolyte ions and make them difficult to penetrate.

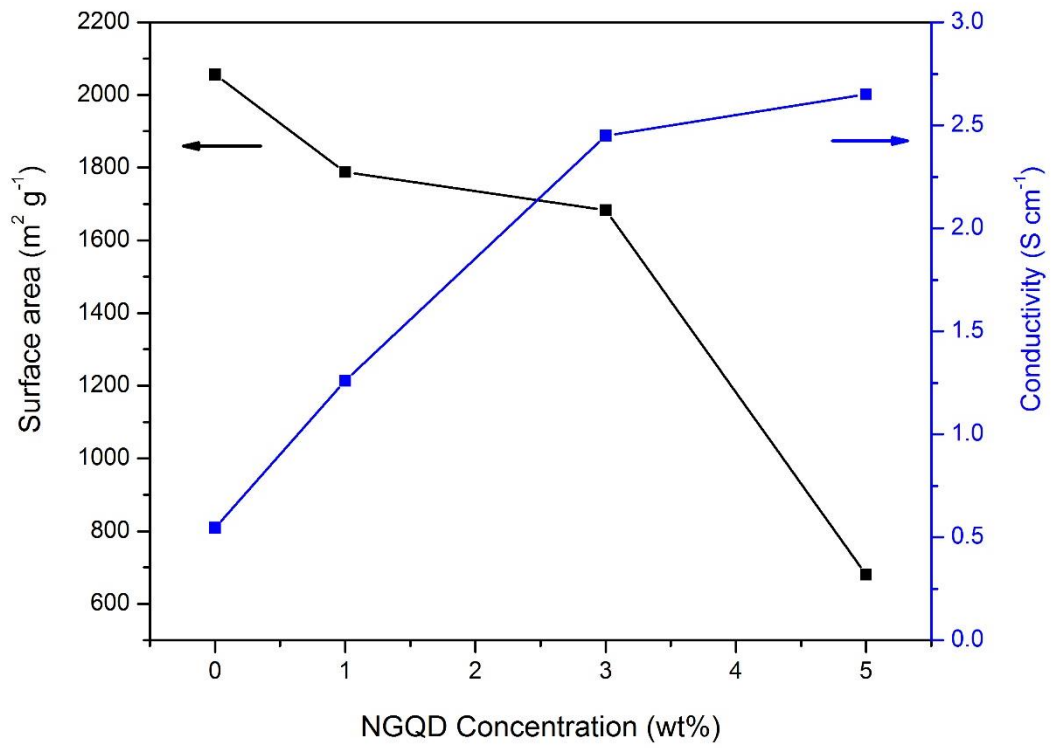


**Figure 14. Specific surface area and conductivity change according to N,S-GQD mass ratio**

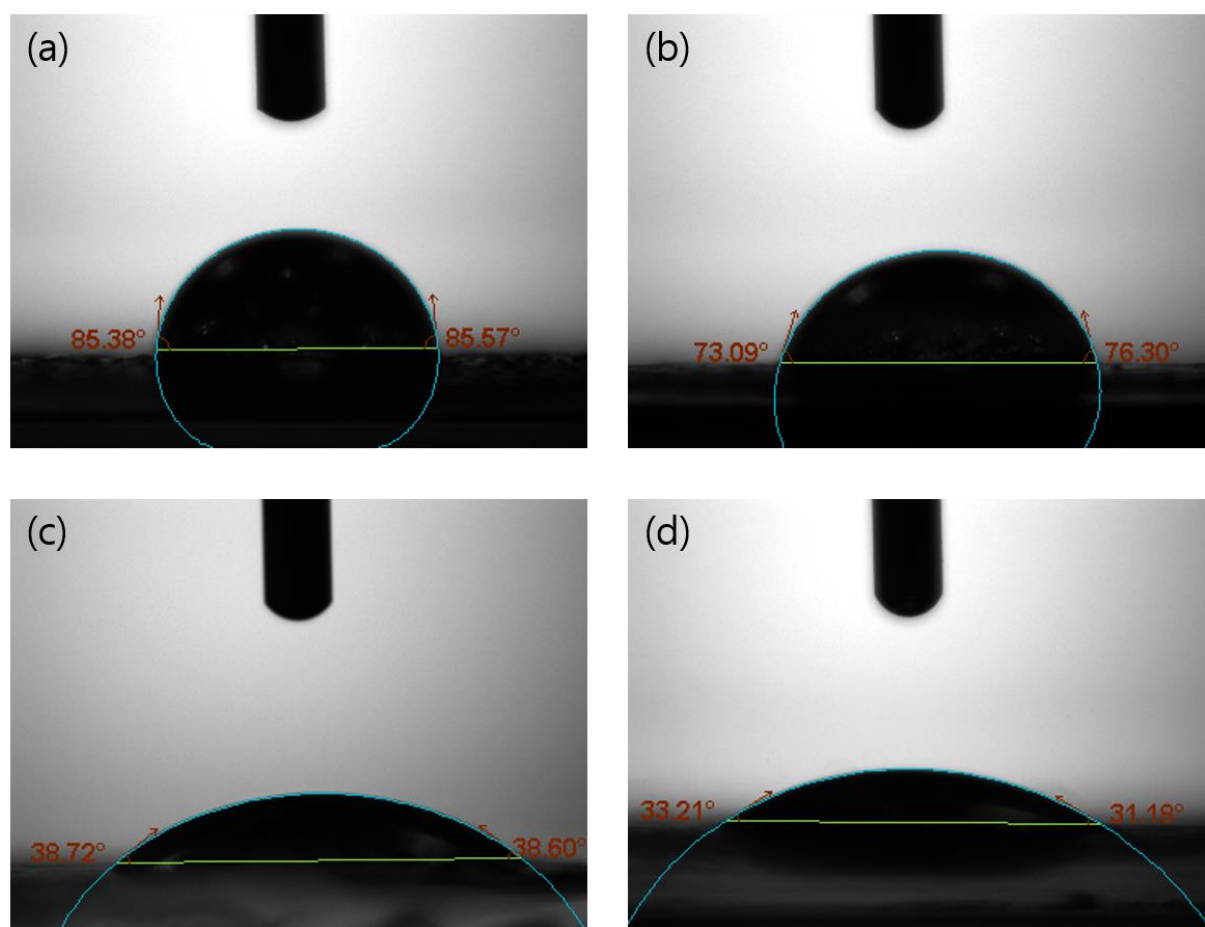


**Figure 15. The contact angle of distilled water on the electrode coated with  
(a) 1:3-600-AC (b) 1wt% N,S-GQD@AC (c) 3wt% N,S-GQD@AC (d) 5wt% N,S-GQD@AC**

**Table 5. The specific surface area of AC obtained at different N,S-GQD mass ratio**

Sample	$S_{\text{BET}}$ ( $\text{m}^2 \text{ g}^{-1}$ )	Pore volume ( $\text{cm}^2 \text{ g}^{-1}$ )
1wt% N,S-GQD@AC	1788	1.267
3wt% N,S-GQD@AC	1683	0.98
5wt% N,S-GQD@AC	704	0.673

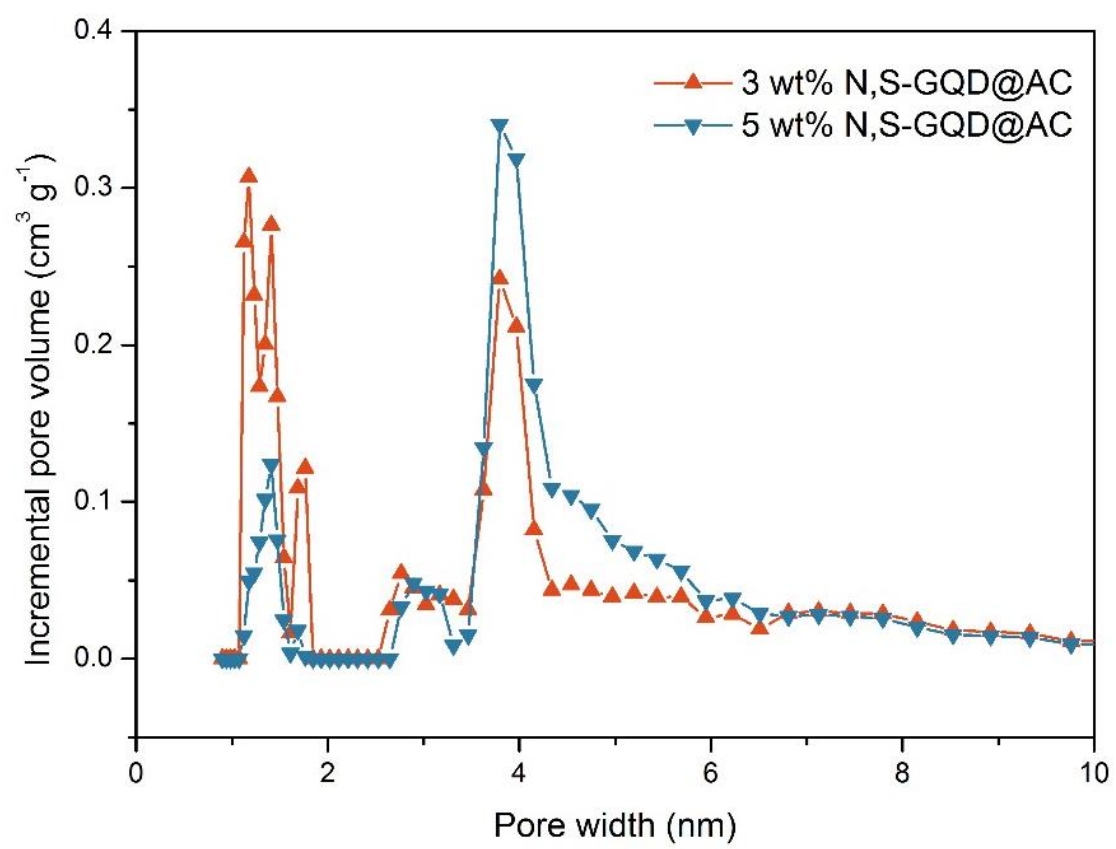


**Figure 16. Pore size distribution of the activated carbon with N,S-GQD**

### **3.3. Chemical characteristics**

XPS analysis was carried out in order to understand the functional groups present on the carbon surfaces. The content of elements and the result of deconvolution of C1s, N1s are given in Table 6, and Table 7. Fig. 17 displays the deconvolution of the XPS signals of C1s and N1s in 1:3-600-AC. Fig. 17 (a) presents the XPS spectra of C1s which were deconvoluted into 6 peaks linked to carbon components namely, C=C (284.38 eV), C-N (285.58 eV), C-O or C-H (286.78 eV), C=O or C=N (288.08 eV), O-C=O (289.28 eV), and  $\pi - \pi^*$  (290.68 eV), respectively. Fig. 17 (b) presents the XPS spectra of N1s reveals four different nitrogen configurations; pyridinic-N (398.18 eV), pyrrolic-N (399.78 eV), Graphitic-N (400.48 eV), and oxidized-N (402.78 eV).

Fig. 18 displays the deconvolution of the XPS signals of C1s and N1s in 8wt% N,S-GQD@AC. Fig. 18 (a) show the XPS spectra of C1s which were deconvoluted into 6 peaks linked to carbon components namely, C=C (284.38 eV), C-N (285.88 eV), C-O or C-H (286.88 eV), C=O or C=N (287.98 eV), O-C=O (289.28 eV), and  $\pi - \pi^*$  (290.58 eV), respectively. Fig. 18 (b) shows the XPS spectra of N1s reveals four different nitrogen configurations; pyridinic-N (398.48 eV), pyrrolic-N (399.88 eV), Graphitic-N (400.98 eV), and oxidized-N (402.38 eV).

**Table 6.** The elemental composition and quantities (wt%) of 1:3-600-AC, N,S-GQD@AC, and N,S-GQDs were obtained from XPS.

Sample	Element content (%)			
	C	O	N	S
1:3-600-AC	87.05	11.49	1.44	-
N,S-GQD@AC	85.21	10.06	2.58	0.53
N,S-GQDs	68.56	18.87	7.44	4.38

**Table 7.** The N and O content (wt%) of 1:3-600-AC, N,S-GQD@AC, and N,S-GQDs obtained from XPS.

Sample	Nitrogen content (%)				Oxygen content (%)	
	Pyridinic N	Pyrrolic N	Graphitic N	Oxidized N	C-O	C=O
1:3-600-AC	0.40	0.49	0.36	0.14	4.82	4.02
N,S-GQD@AC	0.70	1.08	0.52	0.28	4.22	4.82
N,S-GQDs	1.29	4.51	1.64	-	13.93	-

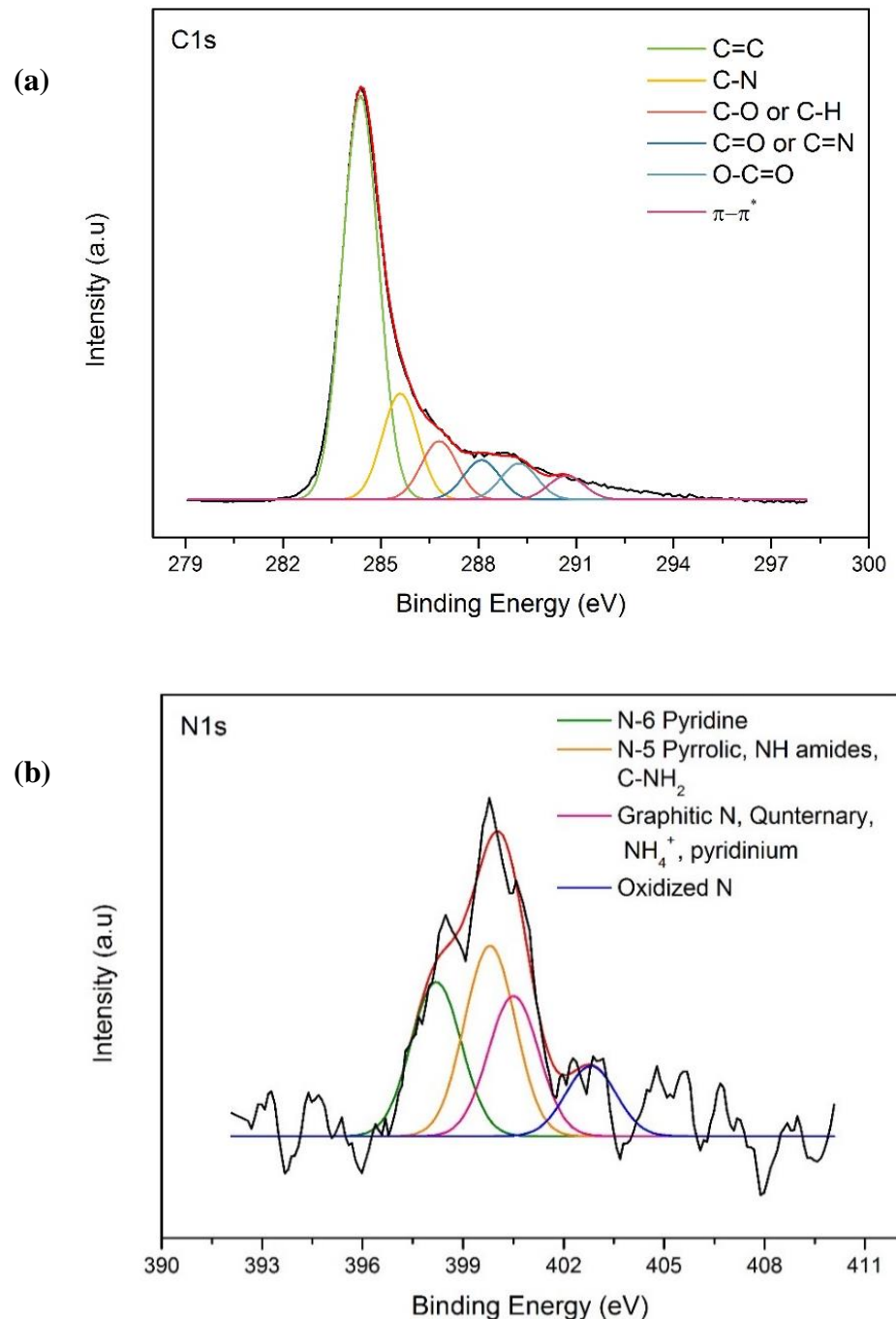
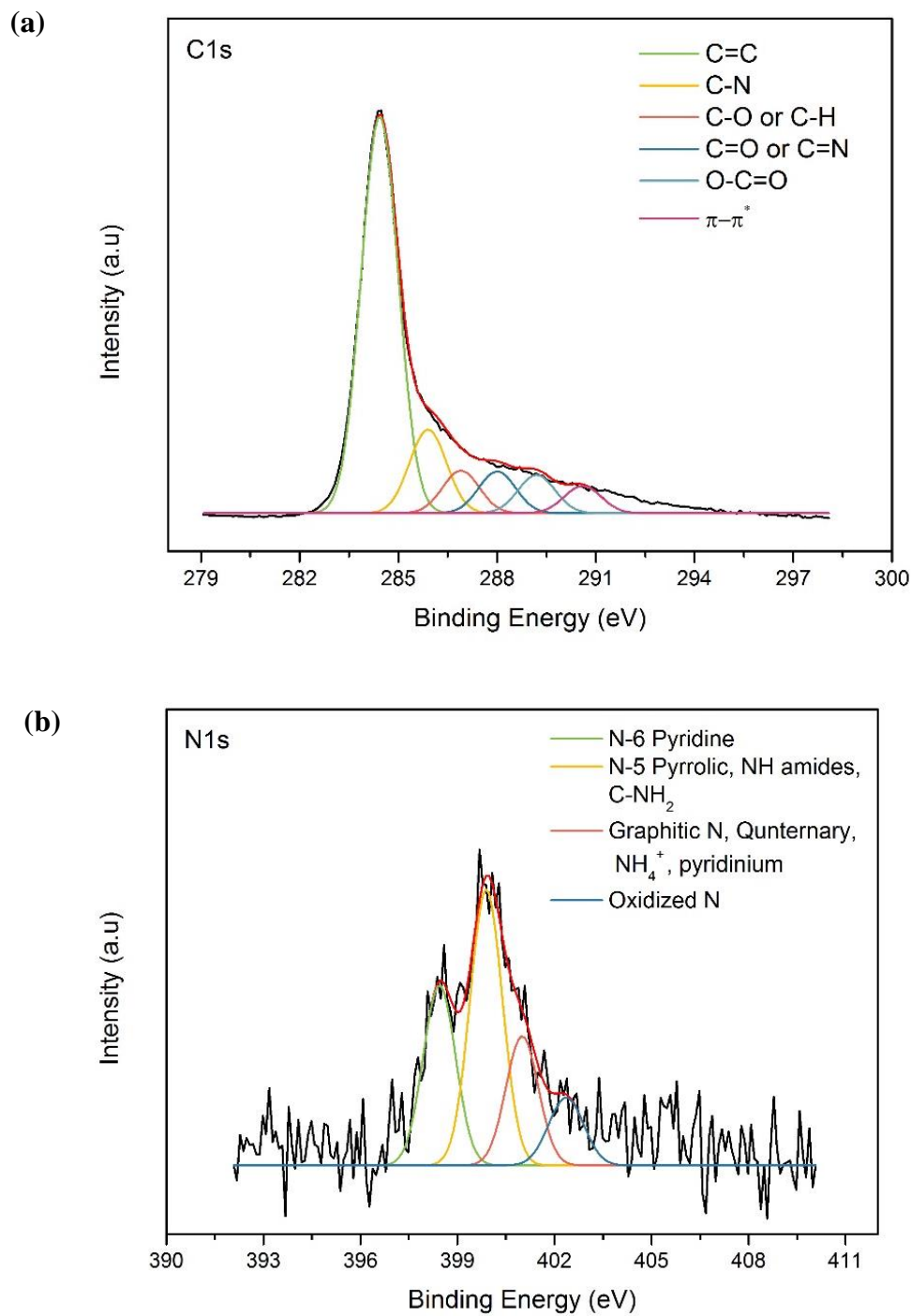


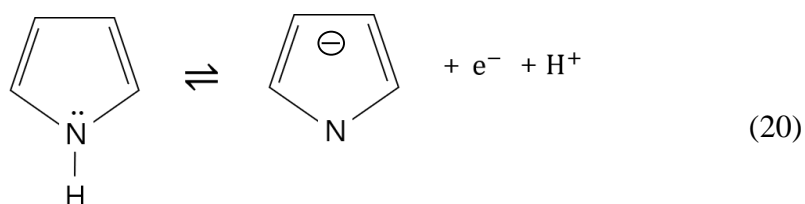
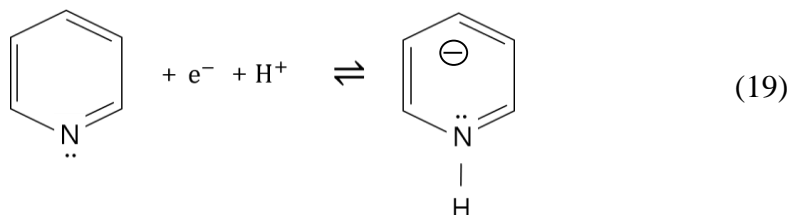
Figure 17. XPS spectra (a) C1s, (b) N1s of 1:3-600-AC



**Figure 18.** XPS spectra (a) C1s, (b) N1s of N,S-GQD@AC

Fig. 19 displays the deconvolution of the XPS signals of C1s and N1s in N,S-GQD. Fig. 19 (a) presents the XPS spectra of C1s which were deconvoluted into 4 peaks linked to carbon components namely, CH<sub>x</sub> (282.88 eV), C=C (284.28 eV), C-N (285.68 eV), and C-O or C-H (286.28 eV), respectively. Fig. 19 (b) presents the XPS spectra of N1s reveals three different nitrogen configurations; pyridinic-N (396.58 eV), pyrrolic-N (398.18 eV), and Graphitic-N (499.58 eV).

Pseudocapacitance is affected by negatively charged groups located at the edges of the carbons, such as pyridinic N and pyrrolic N in N,S-GQDs. In aqueous electrolytes like KOH or H<sub>2</sub>SO<sub>4</sub> solution, pyridinic N and pyrrolic N are prone to reversible redox reactions. Equations (19) and (20) represent the reversible reaction of pyridinic N and pyrrolic N, respectively.



Carbonyl groups (C=O) are also involved in the reversible faradaic redox reactions in aqueous electrolytes. The abundant oxygen-containing groups in the active material, the better wettability, and greater pseudo capacitance can be provided.

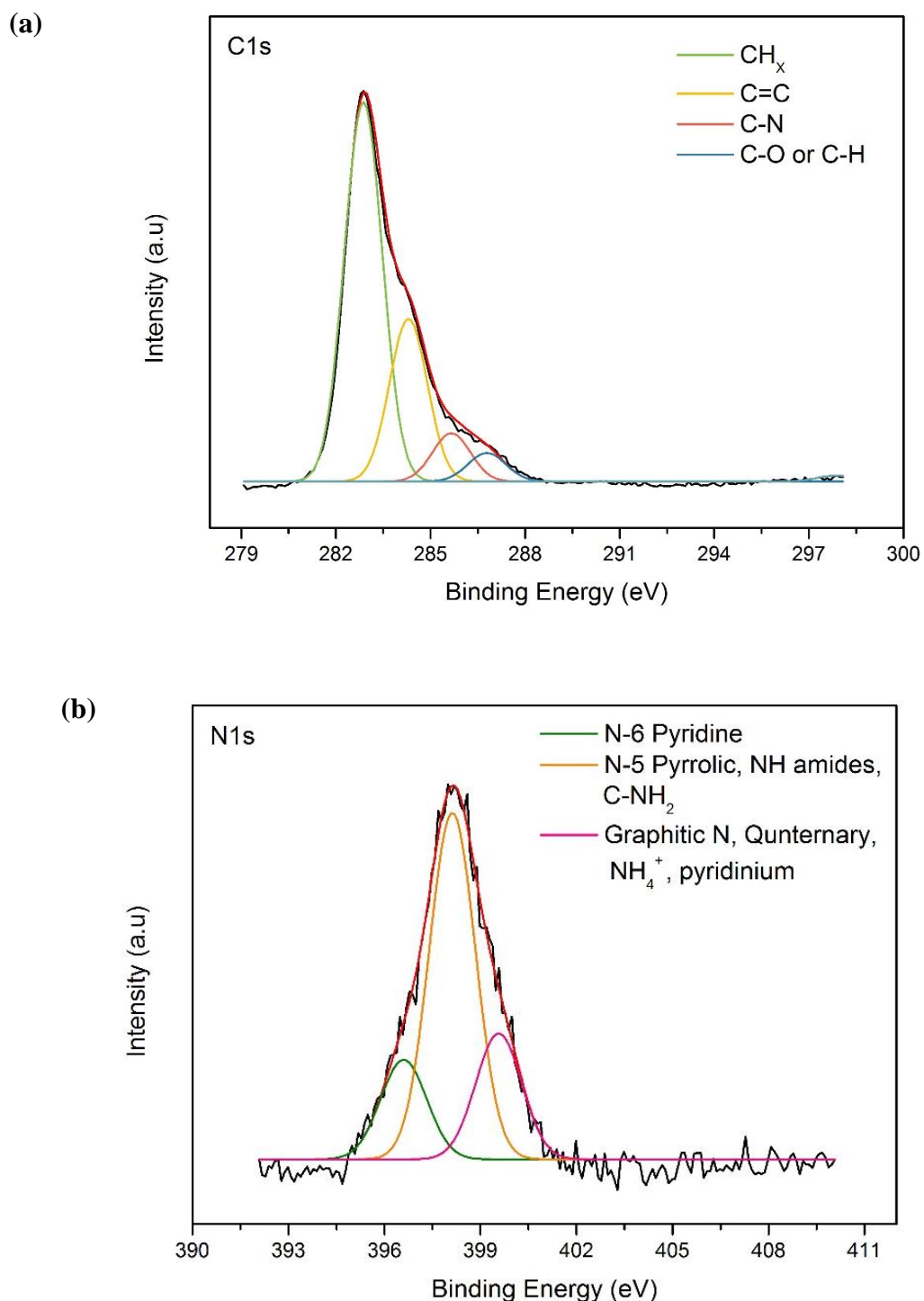
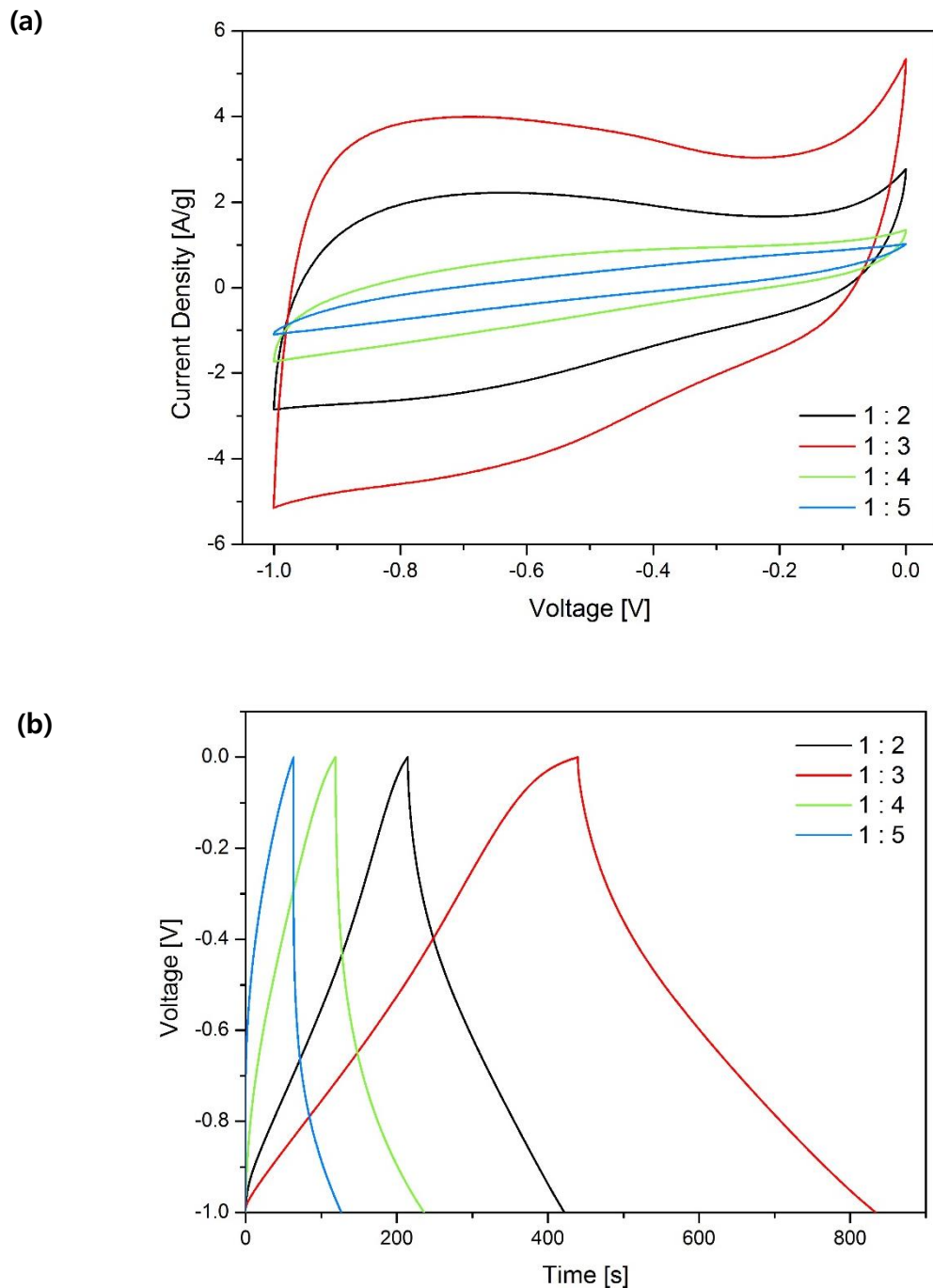


Figure 19. XPS spectra (a) C1s, (b) N1s of N,S-GQD

### **3.4. Electrochemical characteristic**

#### **3.4.1 Three electrode system**

The electrochemical performance of the puffed rice derived activated carbon was analyzed firstly in three-electrode measurement using 6M KOH electrolyte. The samples activated with different KOH mass ratios were measured by cyclic voltammetry (CV) with a scan rate of 10mV/s (Fig. 20 (a)). The N in puffed rice increases paradic pseudo-capacitive activity, making it appear closer to the pseudo-capacitor graph than the ideal rectangular graph. Fig. 20 (b) presents the galvanostatic charge/discharge (GCD) curves at a  $1\text{A g}^{-1}$ . And Table 8 shows the capacitance obtained from GCD of active materials with different KOH ratio. The AC with a PC: KOH mass ratio of 1:3 has the widest specific surface area and therefore provides the highest electrochemical performance ( $343 \text{ F g}^{-1}$ ). The high mass of KOH increases the contact area that reacts with the carbon, which creates a large specific surface area. However, excessive use of KOH causes a lot of activation, resulting in larger pores and reduced surface area. It was confirmed that the specific surface area greatly affects the capacitance. Fig. 21 displays the CV and GCD curves at different scan rates and current densities of 1:3-600-AC.



**Figure 20. Electrochemical performance of AC obtained with different PC and KOH mass ratios (a) CV at 10mV/s scan rate (B) GCD at 1 A g<sup>-1</sup> current density**

**Table 8. The capacitance of AC obtained at different KOH mass ratio**

Sample	Capacitance (F g <sup>-1</sup> )
1:2-600-AC	210
1:3-600-AC	343
1:4-600-AC	117
1:5-600-AC	68

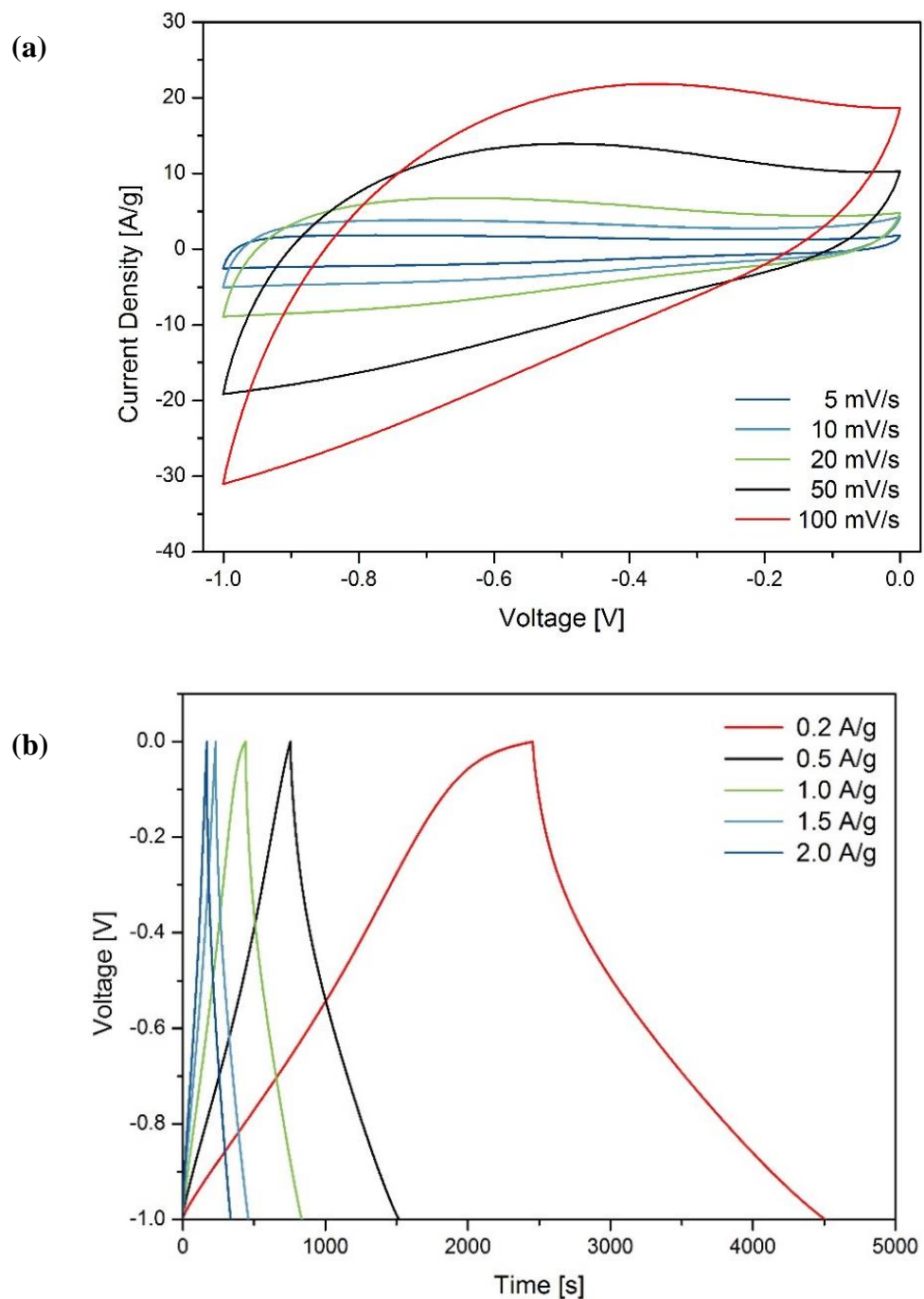


**Figure 21. Electrochemical performance of 1:3-600-AC with 6M KOH electrolyte**  
**(a) CV at different scan rate (B) GCD at different current density**

Fig. 22 (a) and (b) display the CV curves at a scan rate of 10mV/s and the GCD curves at 1A g<sup>-1</sup> for commercial active material (YP-50), 1:3-600-AC, and N,S-GQD@AC. And Table 9 shows the capacitance obtained from GCD of active materials with different N,S-GQD ratio. Despite the widest specific surface area of 1:3-600-AC without N,S-GQD, the active material containing 3wt% of N,S-GQD has the largest capacitance (645 F g<sup>-1</sup>). This is because pyrdinic N and pyrrolic N have a great influence on capacitance as the mass ratio of N in GQDs increases. And N groups not only improves the conductivity and wettability, but also improves the paradic pseudo-capacitance. However, when the N,S-GQD mass ratio increased excessively, the pores were blocked due to N,S-GQDs and the specific surface area decreased, resulting in lower capacitance. CV and GCD curves at different scan rates and current densities of 3wt% N,S-GQD@AC with best performance are shown in Fig. 23.

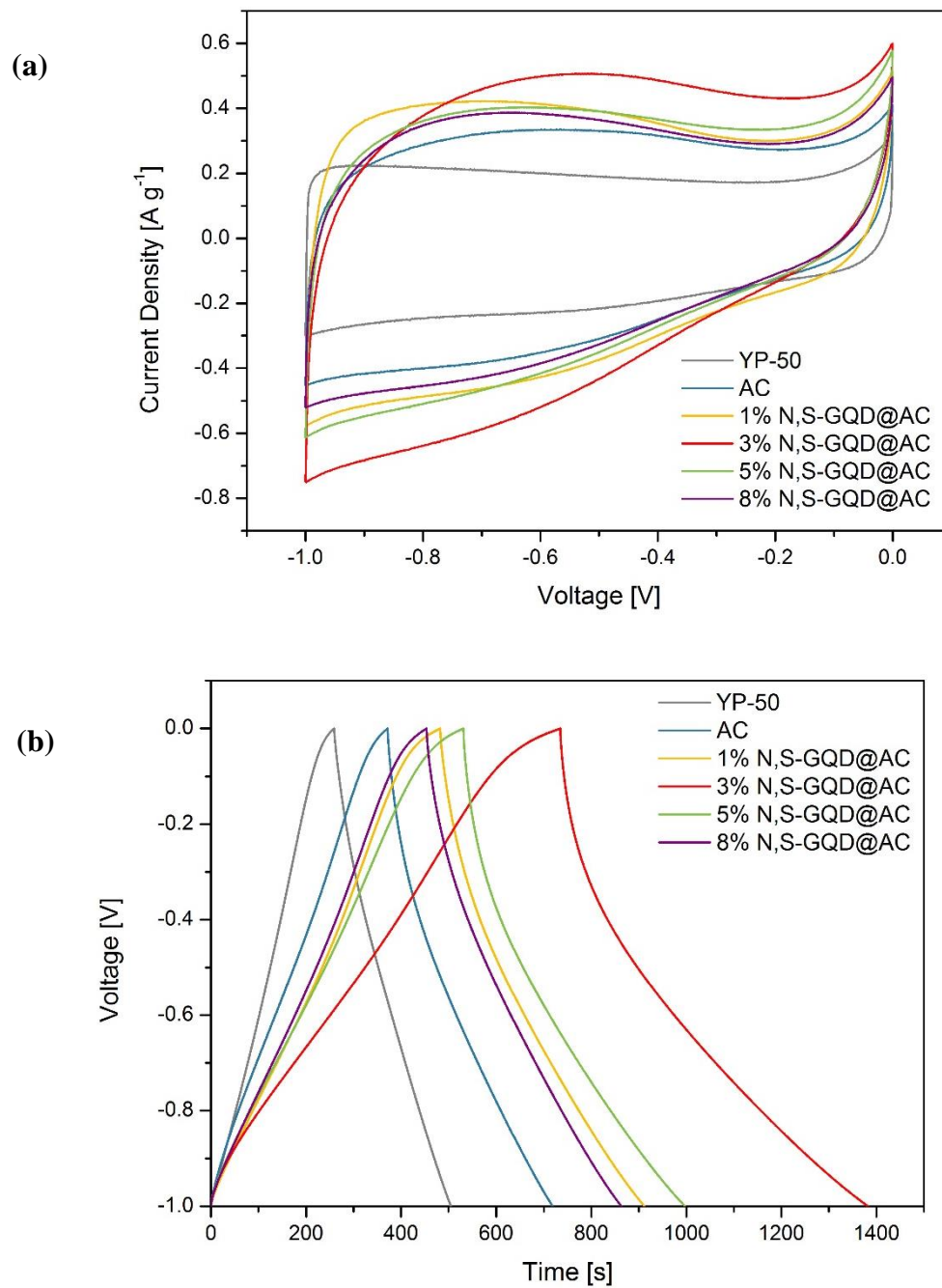


**Figure 22. Electrochemical performance of AC and different N,S-GQD mass ratios with 6M KOH electrolyte (a) CV at 10mV/s scan rate (B) GCD at  $1 \text{ A g}^{-1}$  current density**

**Table 9. The capacitance of AC obtained at different N,S-GQD mass ratio**

Sample	Capacitance (F g <sup>-1</sup> )
YP-50F	250
1wt% N,S-GQD@AC	427
3wt% N,S-GQD@AC	645
5wt% N,S-GQD@AC	466
8wt% N,S-GQD@AC	409

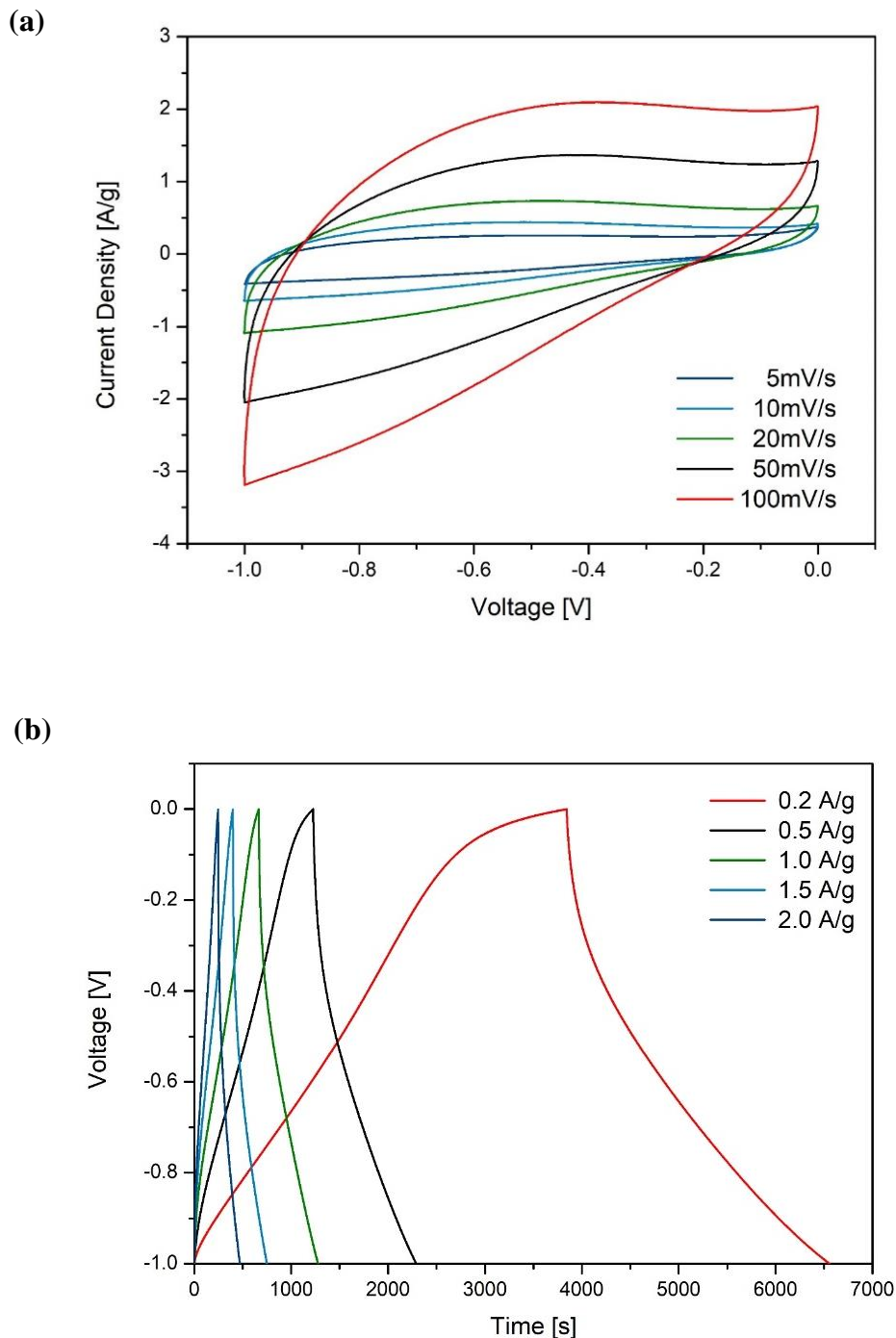


**Figure 23. Electrochemical performance of 3wt% N,S-GQD@AC with 6M KOH electrolyte**  
**(a) CV at different scan rate (b) GCD at different current density**

CV was measured with 1:3-600-AC (without N,S-GQD) and 3wt% N,S-GQD in 3M H<sub>2</sub>SO<sub>4</sub> (Fig. 24). Each sample was measured at a scan rate of 1mV s<sup>-1</sup> in the range of 0V to 0.8V. The CV curve obtained from the 3M H<sub>2</sub>SO<sub>4</sub> electrolyte includes more detail on the contribution of the nitrogen groups than the curve obtained from the 6M KOH electrolyte. Pyrrolic N or pyridinic N caused a redox reaction with the proton in the acidic electrolyte, and a pseudo-capacitance peak was observed between 0.2V to 0.4V. However, in the basic electrolyte, the pseudo-capacitance decreased due to a lack of protons for redox reactions with nitrogen groups. Therefore, the presence of the N functional group of N,S-GQDs in the acidic electrolyte increases the access of protons and makes it possible to have high capacitance.

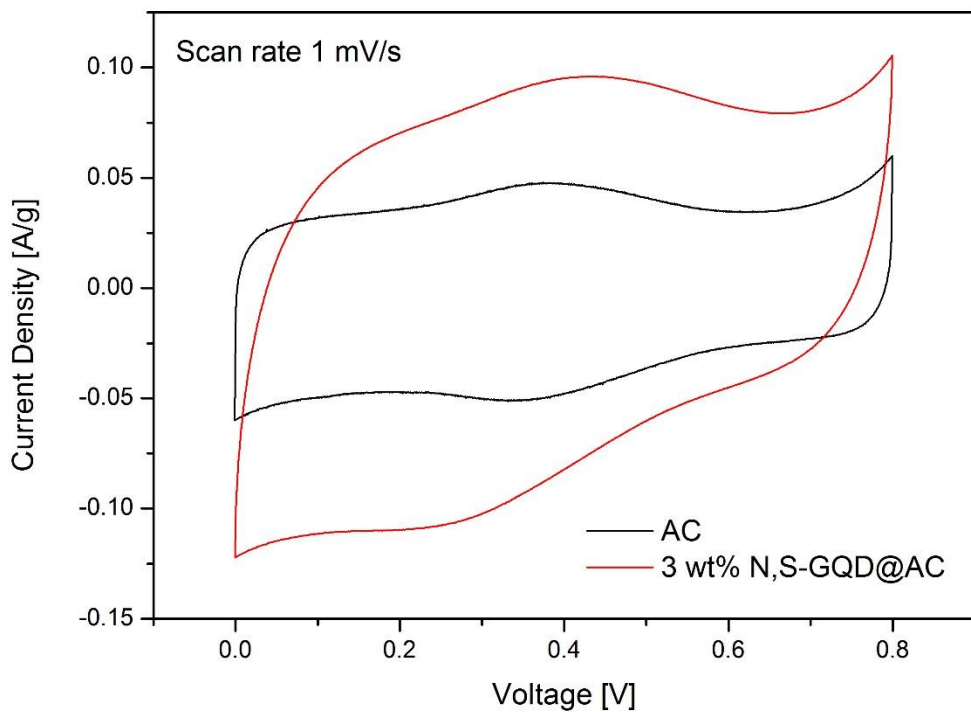


**Figure 24. Electrochemical performance (CV) of 1:3-600-AC and 3wt% N,S-GQD@AC in 3M  $\text{H}_2\text{SO}_4$**

### **3.4.2. Two electrode system**

#### **3.4.2.1. EIS**

Fig. 25 shows the Nyquist plot for the 1:3-600-AC and 3wt% N,S-GQD@AC electrode. The charge transfer resistance ( $R_{ct}$ ) value of 3wt% N,S-GQD@AC electrode is 0.929, which is lower than 1:3-600-AC (3.04). The resistance at the electrode-electrolyte interface is influenced by N,S-GQD and 1:3-600-AC. The presence of N and S heteroatoms of GQD increased the ionic conductivity and the functional groups of O increased the wettability of the electrode. This shows a good electrode-electrolyte interaction and fast ion diffusion occurring at the electrode-electrolyte interface, resulting in low impedance values. A coin cell made of 3wt% N,S-GQD@AC measured Nyquist plots in two cases : at open circuit potential and after repeated charge and discharge of 5,000 cycles in  $1A\ g^{-1}$  (Fig. 26). The charge transfer resistance ( $R_{ct}$ ) after 5,000 cycles is 1.157, showing that it is almost unchanged and stable.

#### **3.4.2.2. Cycle test**

Fig 27 display exhibits the capacity retention of the 1:3-600-AC and 3wt% N,S-GQD@AC. The electrochemical stability for the device using each active material was recorded for up to 5,000 constant galvanostatic charge/discharge cycles at the current density of  $1A\ g^{-1}$ . The electrodes had satisfactory electrochemical stability with capacity retention rates of 95.0% (1:3-600-AC) and 88.8% (3wt% N,S-GQD@AC).

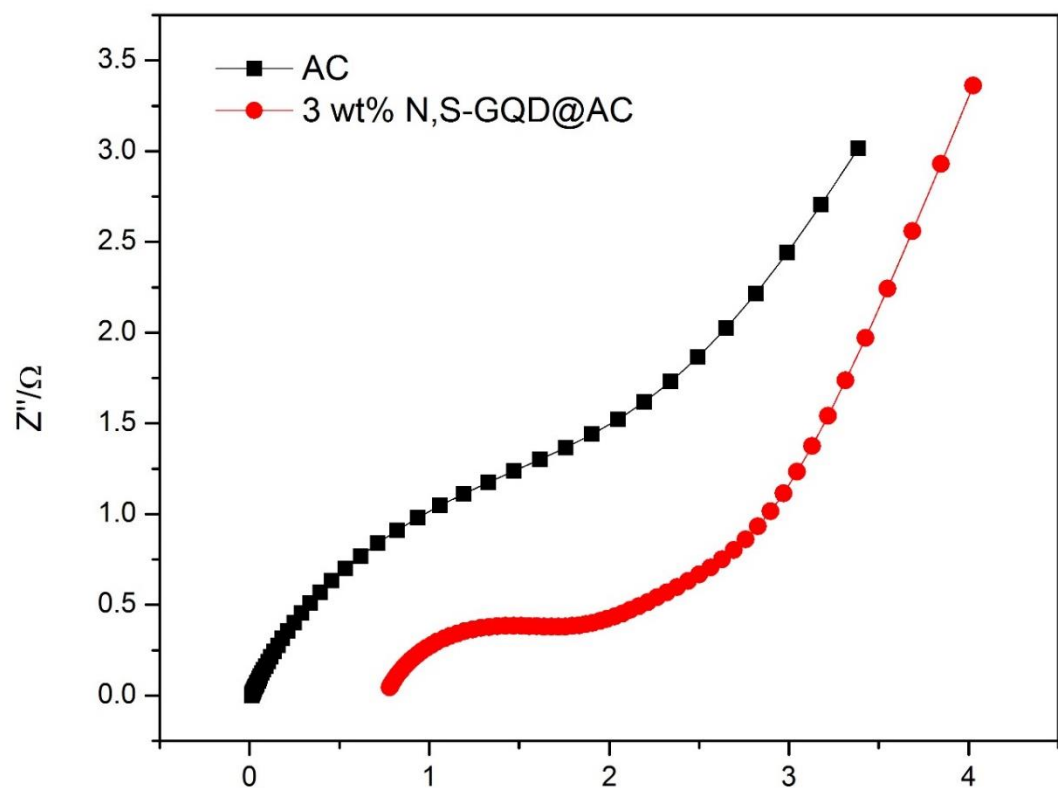


**Figure 25. Nyquist plots of the 1:3-600-AC and 3wt% N,S-GQD@AC with 6M KOH electrolyte**

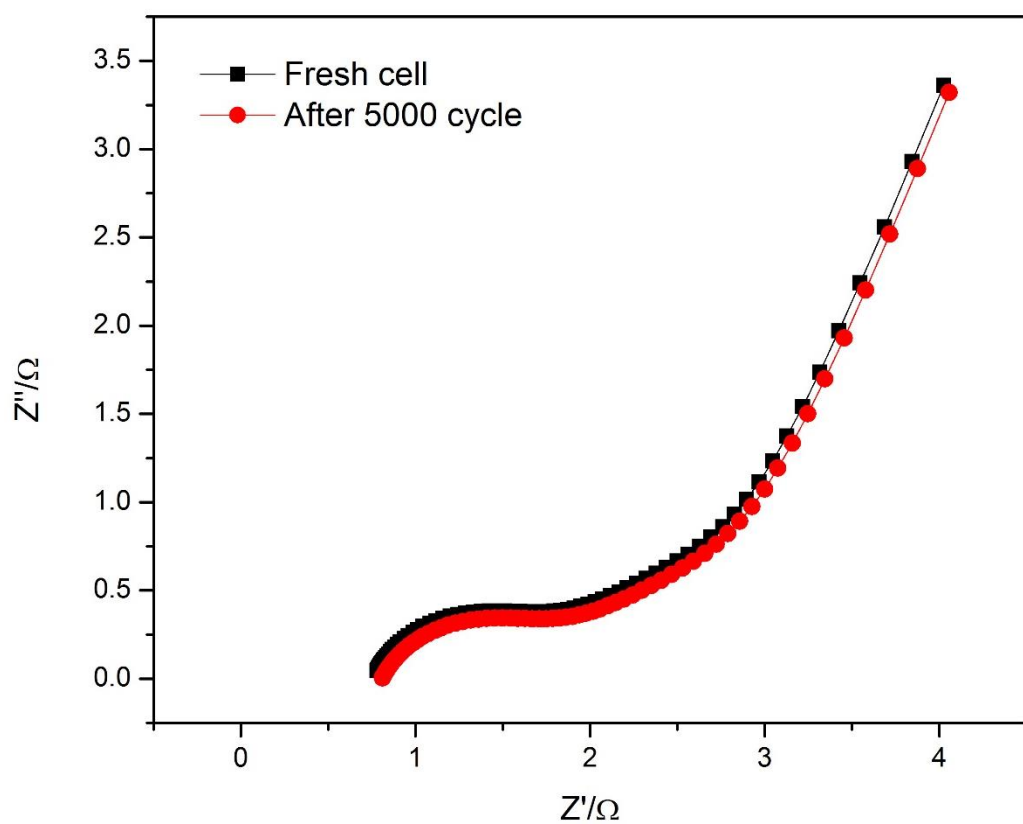


**Figure 26. Nyquist plots in two cases of coin cell with 3wt% N,S-GQD@AC at  $1A g^{-1}$**   
: in open circuit potential and after 5,000 cycle repetitions

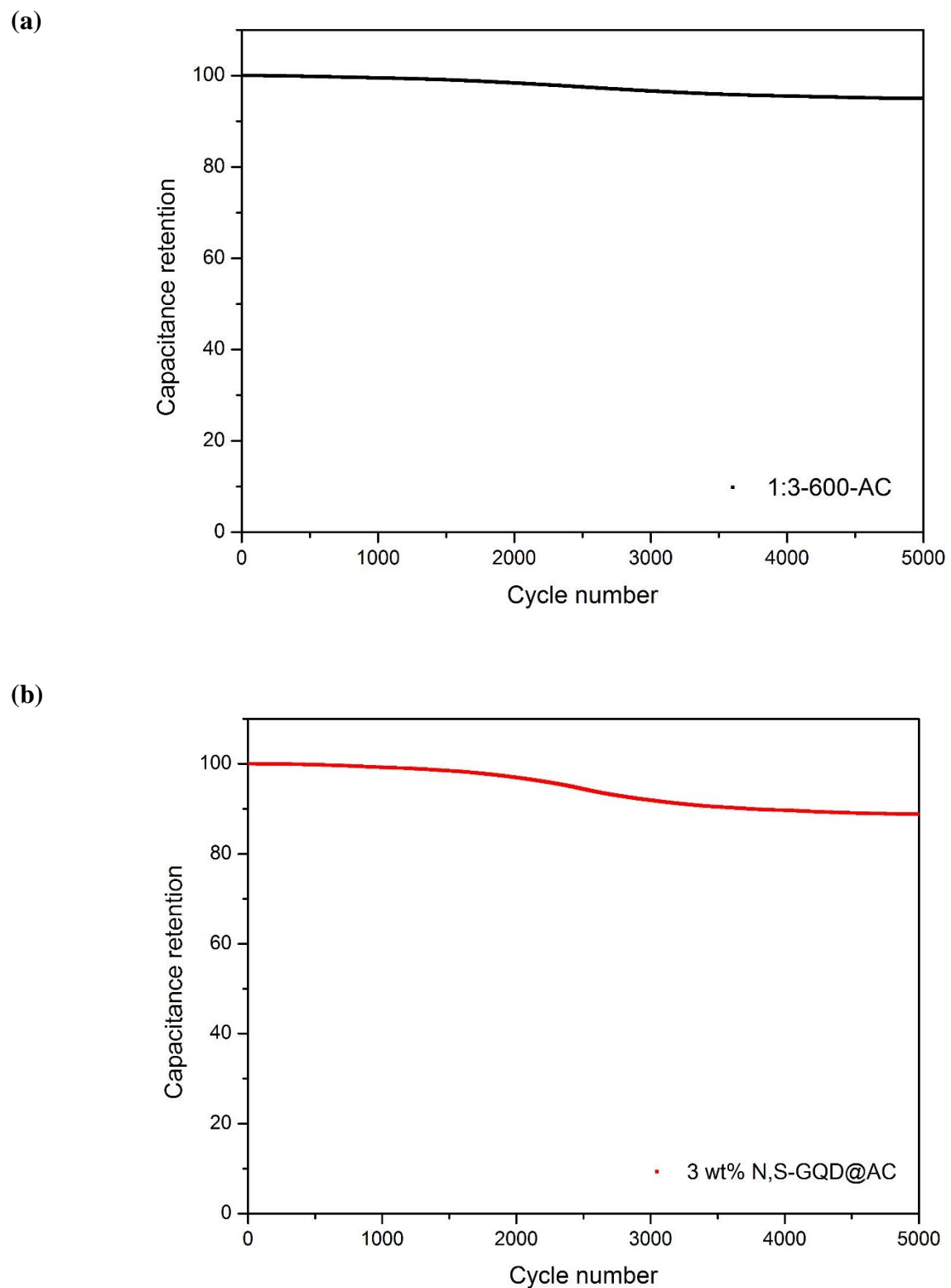


**Figure 27. Cycling performance at current density of  $1\text{A g}^{-1}$**

(a) 1:3-600-AC (b) 3wt% N,S-GQD@AC

### **3.4.3. Flexible supercapacitor**

3wt% N,S-GQD@AC, which showed the best performance, was applied to flexible. The GCD of a flexible supercapacitor at different specific current is shown in Fig. 28. It has  $370\text{F g}^{-1}$  in  $1\text{A g}^{-1}$  and retains 90% capacity even after 10,000 cycles (Fig. 29). Flexibility tests under various bending angles confirmed stable electrochemical performance through the bending and recovery processes (Fig. 30). CV graphs, measured with a scan rate of  $10\text{mV s}^{-1}$  in the range of 0 to 1V, were similar for both flat, fold, and twist angle. Fig. 31 presents a graph of GCD measurement after 1 and 2000 time repetitions of  $180^\circ$  bending. The respective capacitances measured at  $1\text{A g}^{-1}$  are  $374.4\text{ F g}^{-1}$  and  $336.4\text{ F g}^{-1}$ . It has a capacity retention rate of 89.9% after 20,000 repetitions of bending. And we lighted a 1.5V red light emitting diode (LED) with a flexible supercapacitor (Fig. 32). A twisted electrode was used on the left and a folded electrode was used on the right.

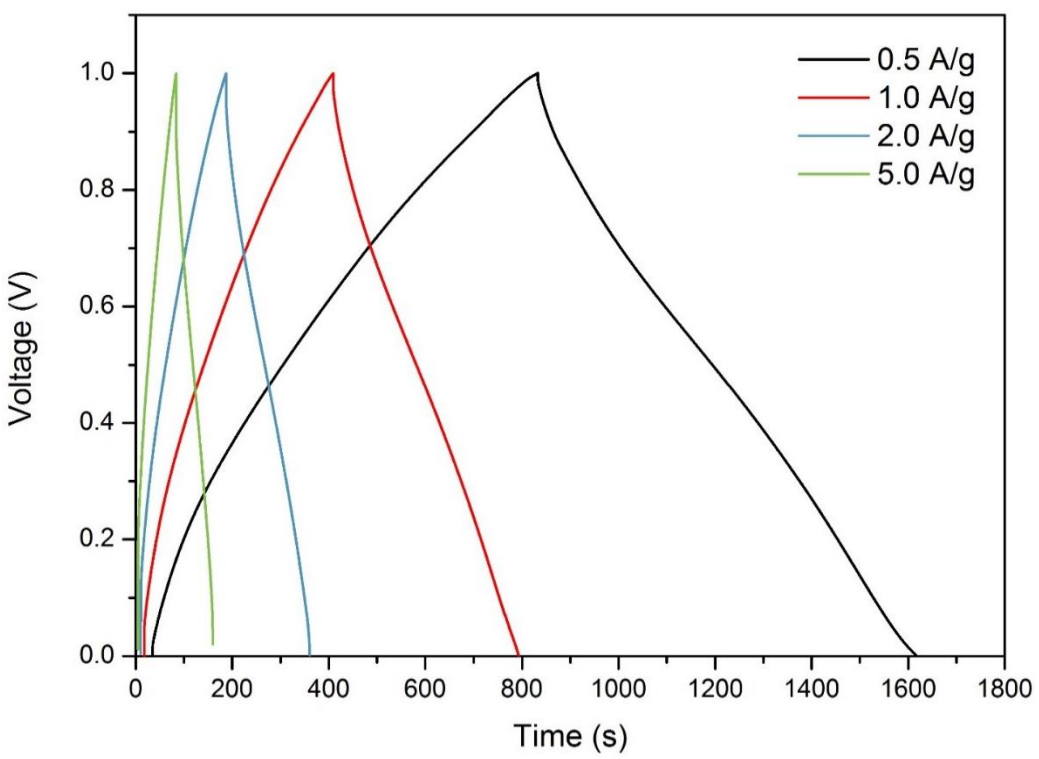


**Figure 28. Electrochemical performance (GCD) of flexible supercapacitor at different current density with 3wt% N,S-GQD@AC**

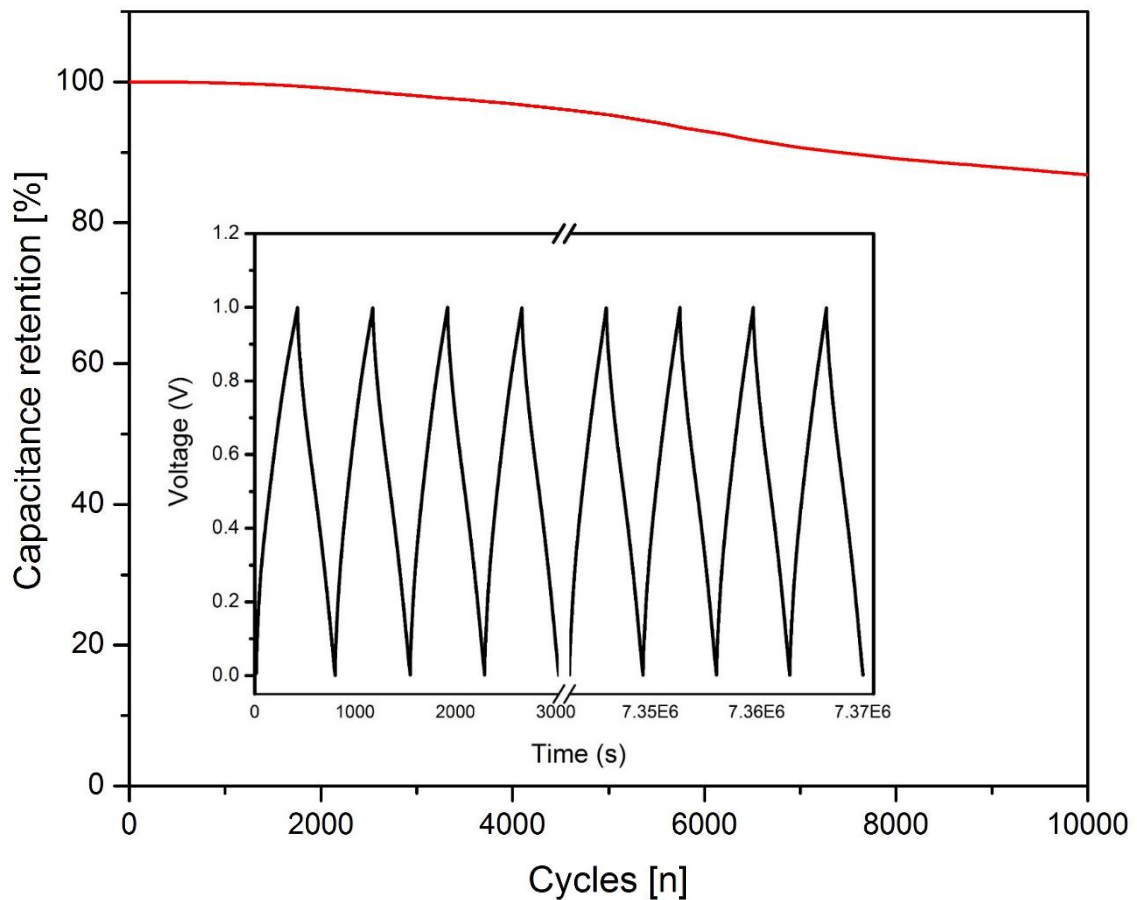


**Figure 29. 10,000 cycle performance (GCD) of flexible supercapacitor at  $1\text{A g}^{-1}$  with 3wt% N,S-GQD@AC**

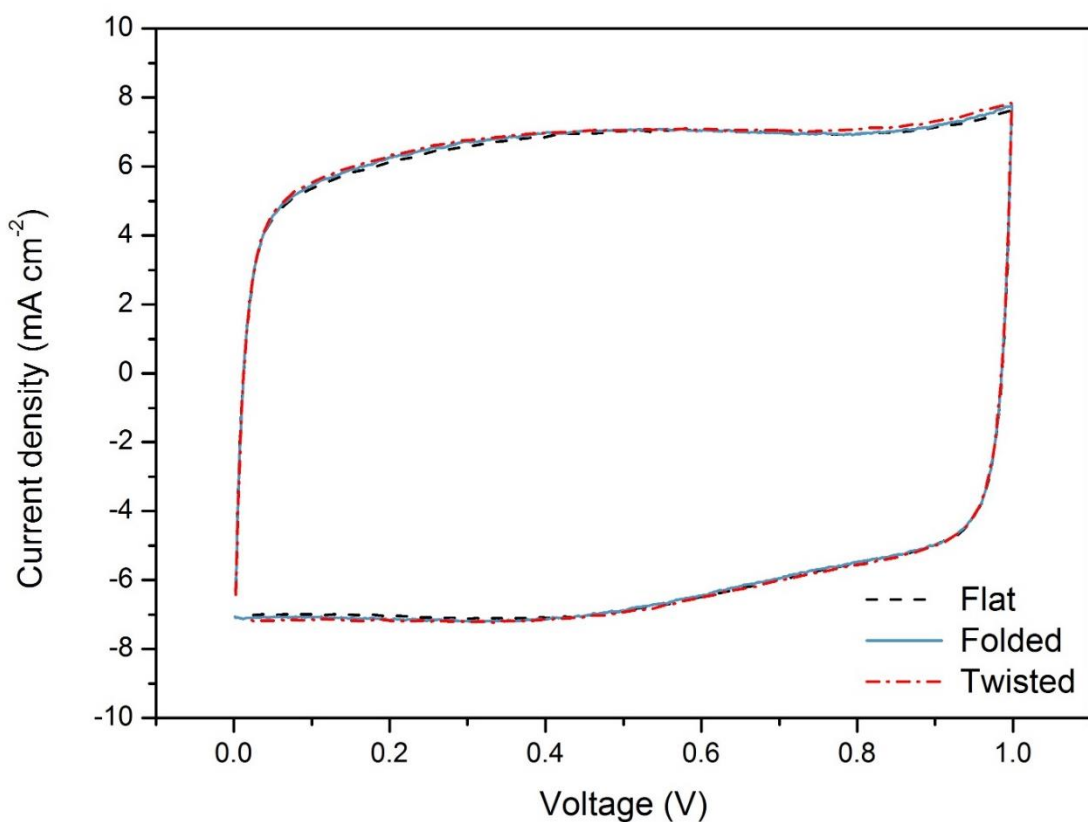


**Figure 30. Different bending angle CV performance graph of the flexible supercapacitor at  $10\text{mV s}^{-1}$**

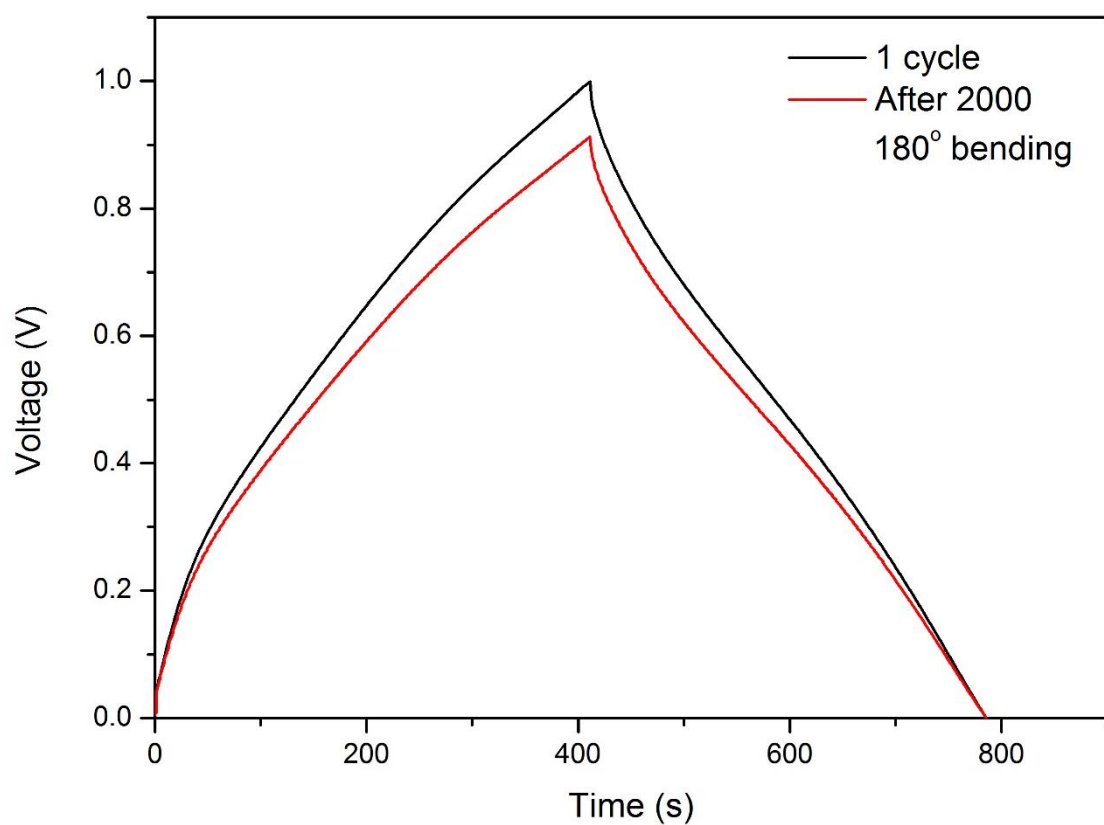


**Figure 31. GCD measurement after 1 and 2,000 time repetitions of 180° bending**



Figure 32. Red light-emitting diode (LED) lighting with flexible supercapacitor

## 4. Conclusion

In this study, two methods were used to improve the performance of the supercapacitor. First, puffed rice was activated and carbonized under a vacuum control to obtain activated carbon having a large specific surface area and maintain a hierarchical micropore structure. This structure helps ion diffusion and allows electrolyte ions to be well adsorbed on the surface of the active material, providing in higher capacitance than commercial active materials. Second, in order to increase the ionic conductivity, N,S-GQD was synthesized by hydrothermal reaction of black soybean milk, which was doped into the puffed rice derived carbon. This reduce the charge transfer resistance between the active material and the electrolyte interface, thereby increasing the accessibility and wettability of electrolyte ions. In addition, the N groups such as pyrrolic N, pyridinic N contribute to the pseudo-capacitance, so that supercapacitor having a high capacitance can be obtained. Also, 3wt% N,S-GQD@AC, which showed the highest performance, was applied to the flexible supercapacitor and it achieved high stability at various angles and repetitive charging and discharging.

Active substances obtained from biomass like puffed rice and black soy milk are expected to contribute to creating flexible devices that are sustainable, environmentally friendly and capable of storing high electrochemical energy at an affordable price.

## 5. Reference

1. Chu, S. and A. Majumdar, *Opportunities and challenges for a sustainable energy future*. Nature, 2012. **488**(7411): p. 294-303.
2. Kabir, E., et al., *Solar energy: Potential and future prospects*. Renewable and Sustainable Energy Reviews, 2018. **82**: p. 894-900.
3. Mohammadi, K., et al., *Electricity Generation and Energy Cost Estimation of Large-Scale Wind Turbines in Jarandagh, Iran*. Journal of Energy, 2014. **2014**: p. 1-8.
4. Zhu, J., et al., *A review of geothermal energy resources, development, and applications in China: Current status and prospects*. Energy, 2015. **93**: p. 466-483.
5. Senthil, C. and C.W. Lee, *Biomass-derived biochar materials as sustainable energy sources for electrochemical energy storage devices*. Renewable and Sustainable Energy Reviews, 2020.
6. Anvari, M., et al., *Short term fluctuations of wind and solar power systems*. New Journal of Physics, 2016. **18**(6).
7. Mirzaeian, M., et al., *Electrode and electrolyte materials for electrochemical capacitors*. International Journal of Hydrogen Energy, 2017. **42**(40): p. 25565-25587.
8. Rozzi, E., et al., *Green Synthetic Fuels: Renewable Routes for the Conversion of Non-Fossil Feedstocks into Gaseous Fuels and Their End Uses*. Energies, 2020. **13**(2).
9. Zhu, J., et al., *Investigation of lithium-ion battery degradation mechanisms by combining differential voltage analysis and alternating current impedance*. Journal of Power Sources, 2020. **448**.
10. Harper, G., et al., *Recycling lithium-ion batteries from electric vehicles*. Nature, 2019. **575**(7781): p. 75-86.
11. Li, F., et al., *Resorcinol-formaldehyde based carbon aerogel: Preparation, structure and applications in energy storage devices*. Microporous and Mesoporous Materials, 2019. **279**: p. 293-315.
12. González, J.F., et al., *Pyrolysis of various biomass residues and char utilization for the production of activated carbons*. Journal of Analytical and Applied Pyrolysis, 2009. **85**(1-2): p. 134-141.
13. Jain, A. and S.K. Tripathi, *Fabrication and characterization of energy storing supercapacitor devices using coconut shell based activated charcoal electrode*. Materials Science and Engineering: B, 2014. **183**: p. 54-60.
14. Prauchner, M.J. and F. Rodríguez-Reinoso, *Chemical versus physical activation of coconut shell: A comparative study*. Microporous and Mesoporous Materials, 2012. **152**: p. 163-171.
15. Jain, A. and S.K. Tripathi, *Nano-porous activated carbon from sugarcane waste for supercapacitor application*. Journal of Energy Storage, 2015. **4**: p. 121-127.
16. Gurten Inal, I.I., et al., *The supercapacitor performance of hierarchical porous activated*

- carbon electrodes synthesised from demineralised (waste) cumin plant by microwave pretreatment.* Journal of Industrial and Engineering Chemistry, 2018. **61**: p. 124-132.
17. Chen, X., R. Paul, and L. Dai, *Carbon-based supercapacitors for efficient energy storage.* National Science Review, 2017. **4**(3): p. 453-489.
18. Augustyn, V., P. Simon, and B. Dunn, *Pseudocapacitive oxide materials for high-rate electrochemical energy storage.* Energy & Environmental Science, 2014. **7**(5).
19. Liu, T., et al., *Polyaniline and polypyrrole pseudocapacitor electrodes with excellent cycling stability.* Nano Lett, 2014. **14**(5): p. 2522-7.
20. Bryan, A.M., et al., *Conducting Polymers for Pseudocapacitive Energy Storage.* Chemistry of Materials, 2016. **28**(17): p. 5989-5998.
21. Torchala, K., K. Kierzek, and J. Machnikowski, *Capacitance behavior of KOH activated mesocarbon microbeads in different aqueous electrolytes.* Electrochimica Acta, 2012. **86**: p. 260-267.
22. Mastragostino, M. and F. Soavi, *Strategies for high-performance supercapacitors for HEV.* Journal of Power Sources, 2007. **174**(1): p. 89-93.
23. Taberna, P.L., C. Portet, and P. Simon, *Electrode surface treatment and electrochemical impedance spectroscopy study on carbon/carbon supercapacitors.* Applied Physics A, 2005. **82**(4): p. 639-646.
24. Vaquero, S., et al., *Insights into the influence of pore size distribution and surface functionalities in the behaviour of carbon supercapacitors.* Electrochimica Acta, 2012. **86**: p. 241-247.
25. Zhang, S.S., *A review on the separators of liquid electrolyte Li-ion batteries.* Journal of Power Sources, 2007. **164**(1): p. 351-364.
26. Zhang, L.L. and X.S. Zhao, *Carbon-based materials as supercapacitor electrodes.* Chem Soc Rev, 2009. **38**(9): p. 2520-31.
27. Bouchelta, C., et al., *Preparation and characterization of activated carbon from date stones by physical activation with steam.* Journal of Analytical and Applied Pyrolysis, 2008. **82**(1): p. 70-77.
28. Bergna, D., et al., *Effect of Some Process Parameters on the Main Properties of Activated Carbon Produced from Peat in a Lab-Scale Process.* Waste and Biomass Valorization, 2019. **11**(6): p. 2837-2848.
29. Sevilla, M. and R. Mokaya, *Energy storage applications of activated carbons: supercapacitors and hydrogen storage.* Energy Environ. Sci., 2014. **7**(4): p. 1250-1280.
30. <[37] Influence of different chemical regents on the preparation of activated carbons from bituminous coal.pdf>.
31. Robau-Sánchez, A., et al., *On the reaction mechanism of the chemical activation of Quercus Agrifolia char by alkaline hydroxides.* Journal of Porous Materials, 2006. **13**(2): p. 123-132.
32. Han, J., et al., *Longitudinal unzipped carbon nanotubes with high specific surface area and*

- trimodal pore structure.* RSC Advances, 2016. **6**(11): p. 8661-8668.
- 33. Kim, C.O., et al., *High-performance graphene-quantum-dot photodetectors.* Sci Rep, 2014. **4**: p. 5603.
  - 34. Subramanian, A., et al., *High-Performance Photodetector Based on a Graphene Quantum Dot/CH<sub>3</sub>NH<sub>3</sub>PbI<sub>3</sub> Perovskite Hybrid.* ACS Applied Electronic Materials, 2019. **2**(1): p. 230-237.
  - 35. Zeng, Z., et al., *Graphene quantum dots (GQDs) and its derivatives for multifarious photocatalysis and photoelectrocatalysis.* Catalysis Today, 2018. **315**: p. 171-183.
  - 36. Kim, J., et al., *Enhancement of Dye-sensitized Solar Cells Efficiency Using Graphene Quantum Dots as Photoanode.* Bulletin of the Korean Chemical Society, 2019. **40**(1): p. 56-61.
  - 37. Luo, P., et al., *Hydrothermal Synthesis of Graphene Quantum Dots Supported on Three-Dimensional Graphene for Supercapacitors.* Nanomaterials (Basel), 2019. **9**(2).
  - 38. Lijuan, K., et al., *Phenylalanine-functionalized graphene quantum dot-silicon nanoparticle composite as an anode material for lithium ion batteries with largely enhanced electrochemical performance.* Electrochimica Acta, 2016. **198**: p. 144-155.
  - 39. Ahirwar, S., S. Mallick, and D. Bahadur, *Electrochemical Method To Prepare Graphene Quantum Dots and Graphene Oxide Quantum Dots.* ACS Omega, 2017. **2**(11): p. 8343-8353.
  - 40. Tian, R., et al., *Facile hydrothermal method to prepare graphene quantum dots from graphene oxide with different photoluminescences.* RSC Advances, 2016. **6**(46): p. 40422-40426.
  - 41. Qi, B.-P., et al., *Solvothermal tuning of photoluminescent graphene quantum dots: from preparation to photoluminescence mechanism.* Journal of Nanoparticle Research, 2018. **20**(2).
  - 42. <bottom up cage opening.pdf>.
  - 43. Dong, Y., et al., *Blue luminescent graphene quantum dots and graphene oxide prepared by tuning the carbonization degree of citric acid.* Carbon, 2012. **50**(12): p. 4738-4743.
  - 44. <bottom up microwave.pdf>.
  - 45. Chung, S., R.A. Revia, and M. Zhang, *Graphene Quantum Dots and Their Applications in Bioimaging, Biosensing, and Therapy.* Adv Mater, 2019: p. e1904362.
  - 46. Zhu, F.Y., et al., *3D nanostructure reconstruction based on the SEM imaging principle, and applications.* Nanotechnology, 2014. **25**(18): p. 185705.
  - 47. <[37] bet.pdf>.
  - 48. Hou, J., et al., *Tunable porous structure of carbon nanosheets derived from puffed rice for high energy density supercapacitors.* Journal of Power Sources, 2017. **371**: p. 148-155.
  - 49. Hou, J., et al., *Popcorn-Derived Porous Carbon Flakes with an Ultrahigh Specific Surface Area for Superior Performance Supercapacitors.* ACS Appl Mater Interfaces, 2017. **9**(36): p. 30626-30634.

50. Sattayarut, V., et al., *Preparation and electrochemical performance of nitrogen-enriched activated carbon derived from silkworm pupae waste*. RSC Advances, 2019. **9**(18): p. 9878-9886.